machines

MDPI

Article

Optimization of Airplane Landing in Crosswind Conditions for Minimum Tire Wear

Stefano Cacciola *,†, Carlo E. D. Riboldi † and Edoardo Generali

Dipartimento di Scienze e Tecnologie Aerospaziali, Politecnico di Milano, Via La Masa 34, 20156 Milan, Italy; carlo.riboldi@polimi.it (C.E.D.R.)

* Correspondence: stefano.cacciola@polimi.it

† These authors contributed equally to this work.

Abstract: Being one of the most critical phases of a flight, landing deserves specific attention, especially when the aircraft is subject to external disturbances such as wind. A notable concern associated with touchdown events, especially when crosswind is present, is tire wear. This work is aimed first at developing a nonlinear flight simulator able to handle the entire landing maneuver in non-null wind conditions, considering the airborne phase, the ground run, and the transition between them. Then, the simulator is included in an optimal process to define the landing technique associated with the minimum tire wear. The methodology is tested in a simulation environment with a realistic model of a reference aircraft, showing that a significant reduction in tire wear can be obtained by optimizing the sideslip angle at touchdown and the lateral–directional controls after the airplane touches the runway with both legs of the main landing gear. The amount of the reduction is highly variable and depends on the landing conditions, e.g., the velocity and glide path angle. It may range from some percentage points up to 45%.

Keywords: landing; flight simulation; tire wear; optimization; crosswind; nonlinear flight dynamics; trim; essential matrix detection

Citation: Cacciola, S.; Riboldi, C.E.D.; Generali, E. Optimization of Airplane Landing in Crosswind Conditions for Minimum Tire Wear. *Machines* **2023**, *11*, 599. https://doi.org/10.3390/machines11060599

Academic Editor: Matthijn B. De Rooij

Received: 21 April 2023
Revised: 24 May 2023
Accepted: 26 May 2023
Published: 1 June 2023

1. Introduction

Landing is one of the most critical phases of a flight because the aircraft is flying at low altitudes and low speeds while external disturbances, most notably wind, may bring the aircraft into dangerous conditions due to the proximity of the terrain [1]. Notwithstanding this fact, the safety of landing maneuvers is ensured by effective and consolidated airport procedures, improved knowledge of weather conditions, and the use of automatic controls for approach and landing.

In addition to all considerations about safety, the forces generated by the contact-impact of the landing gear on the runway during the touchdown phase are the cause of fatigue on the airframe structural subcomponents and significant wear of tires.

The tire wear is even more significant when the airplane lands in crosswind conditions. In fact, the airplane cannot be simultaneously aligned with the runway and in a symmetric flight regime during the airborne phase; hence, it will initially touch the ground with only one leg of the main gear and with an asymmetric attitude, undergoing a lateral drift of the wheels. Clearly, in this scenario, techniques aimed at reducing tire wear may be beneficial for airplane operations and maintenance.

The aim of this work is twofold: firstly, to develop a landing maneuver simulator for a fixed-wing aircraft to be employed in a variety of touchdown scenarios, with special emphasis on crosswind conditions, and secondarily, to study the optimal landing maneuver associated with minimum tire wear.

The definition of optimal trajectories through the minimization of a suitable cost function is a long-standing topic in the literature related to flying machines and many examples of different optimization processes are already available [2–5].

Landing simulation is widely discussed in the literature. In fact, one of the most challenging aspects of modern flight simulators is to reproduce the aircraft–ground interaction during landing, in order to allow the simulation of such a complex maneuver, especially in non-null wind conditions.

In order to formulate a simulator able to handle landing maneuvers, considering both airborne phase and the ground run, one has to develop and integrate multiple models for each subsystem, i.e., the model of the aircraft, the model of the landing gear, including tire dynamics and shock absorbers, and the model of the forces associated with the contact between the tire and the runway. The integrated dynamics of the system should also be linked to an algorithm for detecting the contact between a single leg of the landing gear and the ground.

As far as the landing gear dynamics are concerned, several levels of detail may be considered. Dreier [6] proposes a simplified landing gear linear model, in which tires and shock absorbers are modeled as linear spring-damper systems, with a preloaded force to capture the gas pressure preload. Evans [7] applied this simplified linear model to a real-time flight simulator capable of simulating landing conditions, whereas Wang and Holzapfel [8] considered a rigid tire and a linear elastic shock absorber to study abnormal runway contact conditions.

Even though linear approximations are typically employed for modeling all landing gear elements, it is certainly possible to improve the accuracy of the overall modeling including the nonlinear behavior of some subcomponents, such as shock absorbers, without increasing the overall complexity level of the model. Daniels [9] developed a complete nonlinear simulator of telescopic oleo-pneumatic landing gear, including nonlinearities arising from polytropic gas compression, oil damping, the stroke-dependent discharge coefficient, and the internal stick friction. This highly detailed model was validated against experimental data acquired from A-6 aircraft landing gear.

The interaction between tires and the runway and the modeling of normal and in-plane reaction forces represent a point that deserves specific attention.

Different models for tire dynamics and for the determination of the contact point are analyzed in Yang et al. [10]. The authors concluded that even simple models with low computational costs may provide for good approximations in the case of contact over flat surfaces, even though using more complex models improves the estimation of the tire deformations.

Barnes and Yager [11] developed very effective longitudinal and lateral friction models, extended to large tire yaw angles, which take into account the runway conditions (such as dry, wet, and flooded surfaces), aircraft velocity, and simple tire psychical properties. Since it represents a good compromise between complexity and reliability, this model is suitable for online computations and was subsequently used in Vechtel [12], Vechtel et al. [13] for landing simulations.

A standalone evaluation of landing gear performance may also consider tire shimmy, i.e., an oscillatory phenomenon due to the interaction between tire footprint modification and the wheel plane. Shepherd et al. [14]) considered this phenomenon through a procedure featuring a much higher level of complexity.

Aircraft and landing gear dynamics shall be integrated to perform a complete landing simulation. This fact emphasizes, even more, the need for finding a good compromise between modeling complexity and computational costs, as witnessed by the works of Evans [7], Evans et al. [15], Lei et al. [16], and Wen et al. [17]. In all these works, linear or nonlinear dynamical models of aircrafts are integrated with linearized landing gear dynamics, possibly including simple algorithms for ground contact detection.

Given the scope of the present work, the last aspect to consider is the estimation of tire wear, which represents a problem of great interest for civil aviation [18]. Notwithstanding the apparent complexity of this subject, tire wear is widely studied in many applications, typically connected with the automotive sector, and some simple but effective modeling strategies are already available in the literature [19–21].

Inspired by the previous literature, in this work, a simulator, able to handle the entire landing of a generic aircraft including the airborne phase and ground run, is developed, paying attention to the compromise between model complexity and result accuracy. In particular, a 6-DoF nonlinear model of aircraft, of greater complexity with respect to the one previously proposed by the authors for terminal maneuvers [2,22] and based on the theoretical framework typically adopted in the analysis flight trajectories [4,23], is integrated with a nonlinear landing gear system that considers a linearized dynamics tire and a nonlinear model for the forces exerted by the shock absorbers. The dynamics of the tires are triggered by a essential matrix detection algorithm that works independently on each leg of the landing gear to suitably capture the behavior of the system in case of asymmetric landing scenarios. The tool is then included in an optimization algorithm aimed at evaluating the landing maneuver associated with the minimum tire wear.

This paper is organized according to the following plan. Section 2 deals with the definition of the simulator and considers the modeling and integration of aircraft, tire, and shock absorber subsystems and the algorithm for ground contact detection. The final part of this section is dedicated to the definition of the reference airplane model used in this work, whose data are fully reported in Appendix A. In Section 3, the problem of airplane trim for non-null wind conditions is analyzed. Section 4 deals with the estimation of tire wear during touchdown and with its minimization through the optimization of the landing technique. The results of the optimization of the landing in crosswind conditions for minimum tire wear are reported in Section 5. Finally, Section 6 summarizes the main findings of this work and offers some insights on possible improvements and future developments.

2. Simulation Model

In order to simulate and analyze the airplane landing in crosswind conditions, it is necessary to suitably model the system dynamics during the airborne, touchdown, and ground roll phases, considering the impact of the wind. The airplane is modeled as a rigid body in a three-dimensional domain, whereas the related aerodynamic forces and moments are linearized about a reference condition and rendered through the classical stability and control derivatives, as detailed in Section 2.1. Conventional tricycle landing gear with oleo-pneumatic shock absorbers is linked to the airplane model, as detailed in Section 2.2. Finally, the details of the simulation tool and the reference aircraft model are reported in Sections 2.3 and 2.4.

2.1. Model of the Aircraft

The airplane is modeled as a rigid body in three-dimensional space. To suitably consider the impact of crosswind and highlight all possible couplings between longitudinal– and lateral–directional dynamics, the fully nonlinear form of the equations of motion for rigid bodies is preferred.

As commonly performed, we write the equations of motion in the body frame ($\mathcal{B}$), which is defined as a frame attached to the aircraft in its center of gravity, with unit vectors $\boldsymbol{b}_1$, $\boldsymbol{b}_2$, and $\boldsymbol{b}_3$ coincident, respectively, with the roll (pointing to the aircraft nose), pitch (pointing to the right wing), and yaw (pointing to the down side) axes. Unit vectors $\boldsymbol{b}_1$ and $\boldsymbol{b}_3$ define the symmetry plane of the aircraft. The local horizon frame (NED or $\mathcal{N}$) is again attached to the aircraft center of gravity, and its unit vectors $\boldsymbol{n}_1$, $\boldsymbol{n}_2$, and $\boldsymbol{n}_3$ are constantly pointing towards the local north, local east, and down (i.e., towards the center of the earth) directions. The three-dimensional rotation that transforms triad $\mathcal{N}$ into triad $\mathcal{B}$ is handled through the Euler angles of sequence 3–2–1, i.e., heading ψ, pitch θ, and roll ϕ, organized in vector $\boldsymbol{e}_{321} = \{\phi, \theta, \psi\}^T$. The associated rotation tensor $\boldsymbol{R}_{321}(\boldsymbol{e}_{321})$ has components in $\mathcal{N}$ equal to

$$\boldsymbol{R}_{321}^{\mathcal{N}}(\boldsymbol{e}_{321}) = \\ = \begin{bmatrix} \cos\psi\cos\theta & \cos\psi\sin\theta\sin\phi - \sin\psi\cos\phi & \cos\psi\sin\theta\cos\phi + \sin\psi\sin\phi \\ \sin\psi\cos\theta & \sin\psi\sin\theta\sin\phi + \cos\psi\cos\phi & \sin\psi\sin\theta\cos\phi - \cos\psi\sin\phi \\ -\sin\theta & \cos\theta\sin\phi & \cos\theta\cos\phi \end{bmatrix}. \tag{1}$$

The navigational frame $\overline{\mathcal{N}}$ is parallel to the NED frame but its origin is on the runway threshold. Finally, point G_0 indicates the projection of the airplane center of gravity G on the ground along the third unit vector of the NED frame itself.

The equations of motion, expressed in a barycentric body frame ($\mathcal{B}$), read

$$M\dot{\boldsymbol{v}}^{\mathcal{B}} + \boldsymbol{\omega}^{\mathcal{B}} \times M\boldsymbol{v}^{\mathcal{B}} = \boldsymbol{f}_{\mathrm{a}}^{\mathcal{B}} + \boldsymbol{f}_{\mathrm{g}}^{\mathcal{B}} + \boldsymbol{f}_{\mathrm{r}}^{\mathcal{B}} \tag{2a}$$

$$\boldsymbol{J}_G^{\mathcal{B}}\dot{\boldsymbol{\omega}}^{\mathcal{B}} + \boldsymbol{\omega}^{\mathcal{B}} \times (\boldsymbol{J}_G^{\mathcal{B}}\boldsymbol{\omega}^{\mathcal{B}}) = \boldsymbol{m}_{\mathrm{a}\,G}^{\mathcal{B}} + \boldsymbol{m}_{\mathrm{r}\,G}^{\mathcal{B}}, \tag{2b}$$

where the superscript $(\cdot)^{\mathcal{B}}$ indicates that the components of the vector are expressed in the body frame. In Equation (2), M is the mass of the aircraft, $\boldsymbol{J_G}$ is the inertia tensor expressed with respect to the center of gravity, $\boldsymbol{v}$ is the linear velocity, and $\boldsymbol{\omega}$ is the angular velocity. The terms $\boldsymbol{f}_{\mathrm{a}}$, $\boldsymbol{f}_{\mathrm{g}}$, and $\boldsymbol{f}_{\mathrm{r}}$ indicate, respectively, aerodynamic, gravity, and reaction forces, and $\boldsymbol{m}_{G\mathrm{a}}$ and $\boldsymbol{m}_{G\mathrm{r}}$ indicate aerodynamic and reaction moments about the center of gravity G. The gravitational force in the body frame is easily expressed as

$$\boldsymbol{f}_{\mathrm{g}}^{\mathcal{B}} = \left(\boldsymbol{R}_{321}^{\mathcal{N}}\right)^{T} \boldsymbol{f}_{\mathrm{g}}^{\mathcal{N}} = \left(\boldsymbol{R}_{321}^{\mathcal{N}}\right)^{T} \begin{Bmatrix} 0 \\ 0 \\ Mg \end{Bmatrix} = Mg \begin{Bmatrix} -\sin(\theta) \\ \cos(\theta)\sin(\phi) \\ \cos(\theta)\cos(\phi) \end{Bmatrix}, \tag{3}$$

while the moment of the gravitational force about the center of gravity is null by definition.

The models of the aerodynamic forces and moments are linearized about a suitable reference condition and rendered through the stability and control derivatives. As usual, they are expressed in terms of the linear and angular velocities, deflections of the control surfaces, thrust throttle, and rate of the linear velocities. The effect of the wind speed $\boldsymbol{v}_{\mathrm{w}}$ should be also included in the modeling of aerodynamics. To this end, we may introduce the vectorial relationship between the ground speed $\boldsymbol{v}$, wind speed, $\boldsymbol{v}_{\mathrm{w}}$ and airspeed $\boldsymbol{v}_{\mathrm{a}}$,

$$\boldsymbol{v} = \boldsymbol{v}_{\mathrm{a}} + \boldsymbol{v}_{\mathrm{w}}. \tag{4}$$

Notice that the aerodynamic angles, i.e., the angle of attack α and sideslip β, are defined considering the airspeed (not the ground speed), which is viewed in the body frame as

$$\alpha = \arctan\left(\frac{v_{\mathrm{a}\,3}^{\mathcal{B}}}{v_{\mathrm{a}\,1}^{\mathcal{B}}}\right), \quad \beta = \arcsin\left(\frac{v_{\mathrm{a}\,2}^{\mathcal{B}}}{|\boldsymbol{v}_{\mathrm{a}}|}\right), \tag{5}$$

where $v_{\mathrm{a}\,1}^{\mathcal{B}}$, $v_{\mathrm{a}\,2}^{\mathcal{B}}$, and $v_{\mathrm{a}\,3}^{\mathcal{B}}$ are the three components of the airspeed in the body frame. In contrast, the trajectory angles (i.e., the track angle χ and climb angle γ) are defined according to the ground speed, which is viewed in the NED frame as

$$\chi = \arctan\left(\frac{v_2^{\mathcal{N}}}{v_1^{\mathcal{N}}}\right), \quad \gamma = -\arcsin\left(\frac{v_3^{\mathcal{N}}}{|\boldsymbol{v}|}\right), \tag{6}$$

where $v_1^{\mathcal{N}}$, $v_2^{\mathcal{N}}$, and $v_3^{\mathcal{N}}$ are the three components of the ground speed in the NED frame. As a founding hypothesis, the wind is considered constant over time and uniform over space.

Accordingly, aerodynamic forces and moments are

$$\boldsymbol{f}_{\mathrm{a}} = \boldsymbol{f}_{\mathrm{a}_{\mathrm{ref}}} + \begin{bmatrix} \frac{\partial \boldsymbol{f}_{\mathrm{a}}}{\partial \boldsymbol{v}} & \frac{\partial \boldsymbol{f}_{\mathrm{a}}}{\partial \boldsymbol{\omega}} & \frac{\partial \boldsymbol{f}_{\mathrm{a}}}{\partial \boldsymbol{\delta}} & \frac{\partial \boldsymbol{f}_{\mathrm{a}}}{\partial \dot{\boldsymbol{v}}} \end{bmatrix} \begin{Bmatrix} \boldsymbol{v} - \boldsymbol{v}_{\mathrm{W}} - \boldsymbol{v}_{\mathrm{a}_{\mathrm{ref}}} \\ \boldsymbol{\omega} - \boldsymbol{\omega}_{\mathrm{ref}} \\ \boldsymbol{\delta} - \boldsymbol{\delta}_{\mathrm{ref}} \\ \dot{\boldsymbol{v}} - \dot{\boldsymbol{v}}_{\mathrm{a}_{\mathrm{ref}}} \end{Bmatrix} \tag{7a}$$

$$\boldsymbol{m}_{\mathrm{a}G} = \boldsymbol{m}_{\mathrm{a}G\mathrm{ref}} + \begin{bmatrix} \frac{\partial \boldsymbol{m}_{\mathrm{a}G}}{\partial \boldsymbol{v}} & \frac{\partial \boldsymbol{m}_{\mathrm{a}G}}{\partial \boldsymbol{\omega}} & \frac{\partial \boldsymbol{m}_{\mathrm{a}G}}{\partial \boldsymbol{\delta}} & \frac{\partial \boldsymbol{m}_{\mathrm{a}G}}{\partial \dot{\boldsymbol{v}}} \end{bmatrix} \begin{Bmatrix} \boldsymbol{v} - \boldsymbol{v}_{\mathrm{W}} - \boldsymbol{v}_{\mathrm{a}_{\mathrm{ref}}} \\ \boldsymbol{\omega} - \boldsymbol{\omega}_{\mathrm{ref}} \\ \boldsymbol{\delta} - \boldsymbol{\delta}_{\mathrm{ref}} \\ \dot{\boldsymbol{v}} - \dot{\boldsymbol{v}}_{\mathrm{a}_{\mathrm{ref}}} \end{Bmatrix} \tag{7b}$$

where $(\cdot)_{\mathrm{ref}}$ denotes values associated with the reference conditions, while the throttle position δ_{T} and elevator δ_{E}, aileron δ_{A}, and rudder δ_{R} deflections are collected in array $\boldsymbol{\delta} = \{\delta_{\mathrm{T}}, \delta_{\mathrm{E}}, \delta_{\mathrm{A}}, \delta_{\mathrm{R}}\}^T$. As a convention, the δ_{E} is positive for upwards elevator deflection (positive pitching moment), the δ_{A} is positive for right aileron upwards deflection (positive rolling moment), and the δ_{R} is positive for leftwards rudder deflection (negative yawing moment). Finally, $\frac{\partial \boldsymbol{f}_{\mathrm{a}}}{\partial \boldsymbol{\xi}}$ and $\frac{\partial \boldsymbol{m}_{\mathrm{a}G}}{\partial \boldsymbol{\xi}}$ represent the classical aerodynamic stability and control derivatives, taken with respect to a generic variable ξ. In general, the aerodynamic matrices feature a chessboard structure, with many zeros where there are elements that link longitudinal variables (e.g., longitudinal velocity and pitch rate) with lateral–directional forces and moments (e.g., side force, roll, and yawing moments) or lateral–directional variables with longitudinal forces and moments. This assumption, normally used in flight mechanics problems, is surely valid for symmetric flights. However, as the sideslip angle increases, the misaligned flow around the entire aircraft may entail an increase in the drag and a general variation in the whole set of longitudinal stability and control derivatives. This effect can be considered rather small if the sideslip angles are small, such as the ones considered in this work. This is particularly true if one analyzes the contribution of the landing gear, which is not aerodynamic and hence is less sensitive to small deviations in the flow.

Reaction forces $\boldsymbol{f}_{\mathrm{r}}$ and moments $\boldsymbol{m}_{G\mathrm{r}}$ are only present when the aircraft is in contact with the ground, and their expression will be detailed in Section 2.2.

Finally, the evolution in time of Euler angles is described by

$$\dot{\boldsymbol{e}}_{321} = {\boldsymbol{S}_{321}^{\mathcal{B}}}^{-1} \boldsymbol{\omega}^{\mathcal{B}} \tag{8}$$

where tensor $\boldsymbol{S}_{321}^{\mathcal{B}}$ is defined as

$$\boldsymbol{S}_{321}^{\mathcal{B}} = \begin{bmatrix} 1 & 0 & -\sin\theta \\ 0 & \cos\phi & \cos\theta\sin\phi \\ 0 & -\sin\phi & \cos\theta\cos\phi \end{bmatrix}. \tag{9}$$

The position of the aiplane center of gravity $\boldsymbol{x}_G$ in the navigational frame can be integrated along with Equations (2) and (9), through the knowledge of its derivative

$$\dot{\boldsymbol{x}_G}^{\overline{\mathcal{N}}} = \boldsymbol{R}_{321}^{\mathcal{N}} \boldsymbol{v}^{\mathcal{B}}. \tag{10}$$

Notice that the third component of $\boldsymbol{x}^{\overline{\mathcal{N}}}$ corresponds to the opposite of the airplane altitude, as it can be inferred from Figure 1. Such information will be used when it comes to defining the algorithm for tire–wheel contact detection.

2.2. Model of the Landing Gear

The interaction of the aircraft with the ground is rendered through a simple model of the landing gear linked with an algorithm to determine whether one or more landing gear wheels are in contact with the ground.

In order to have a simple but still accurate modeling, the following assumptions are made:

- Only tricycle landing gear forms are considered, with oleo-pneumatic shock absorbers on main and nose gear (one per leg);
- The direction of the shock absorber deflection is always parallel to the $z_{\mathcal{B}}$ axis;
- Independently of the number of wheels on each landing gear leg, an *equivalent single tire per leg* is considered. Furthermore, the wheel axle is located at the free end of the shock absorber;
- The steering capability of the nose gear is not modeled;
- The rolling dynamics of tires and spin-up loads are neglected;
- A flat and steady Earth is considered. Additionally, the landing surface does not move and is horizontal.

To easily describe ground contact dynamics, as performed by Lei et al. [16], the strut $\overline{\mathcal{S}}$ and the tire $\mathcal{T}$ reference frames are introduced.

The strut frame origin $O_{\overline{\mathcal{S}}}$ is located at the point on which the shock absorber is linked to the fuselage. Frame $\overline{\mathcal{S}}$ is obtained by translating frame $\mathcal{B}$. The tire frame $\mathcal{T}$ origin $O_{\mathcal{T}}$ is located at the geometric center of the wheel. Unit vectors $\boldsymbol{t}_1$ and $\boldsymbol{t}_2$ define a plane parallel to the Earth's surface, while $\boldsymbol{t}_3$ points towards the center of the Earth. As no tire steering angle is considered, $\boldsymbol{t}_1$ remains parallel to the projection of $\boldsymbol{b}_1$ on the Earth's tangent plane, with $\boldsymbol{t}_2$ forming a right-hand triad. Figure 1 schematically shows both frames and the related variables of interest are schematically shown in Figure 1, which also displays body, NED, and navigational frames along with the airplane center of gravity G and its projection onto the ground named G_0.

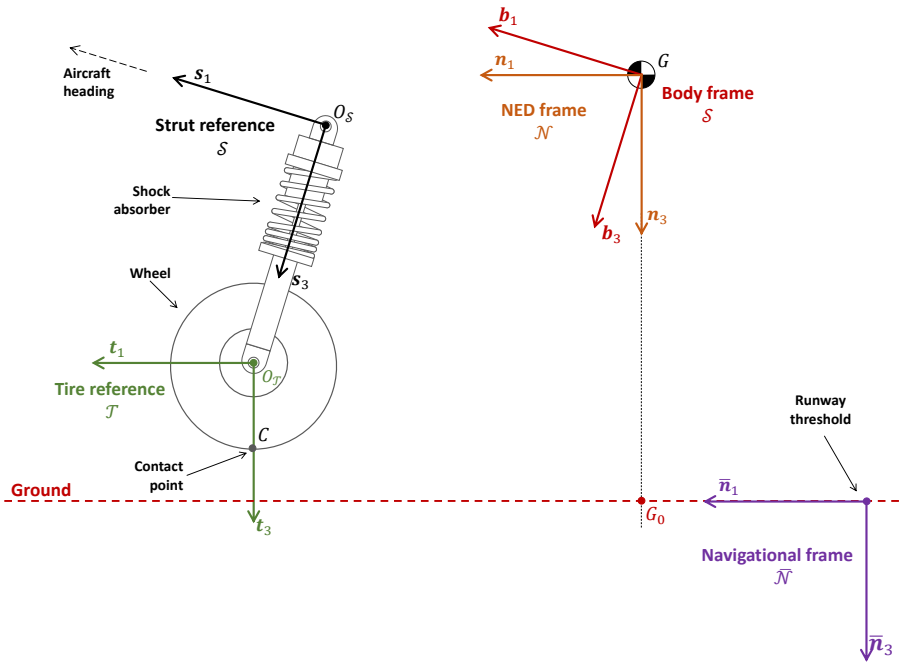

Figure 1. Airplane and landing gear reference frames.

2.2.1. Tire Model

Tire dynamics are included in the model through a straightforward mass-spring-damper system, whose equivalent stiffness and equivalent damping are termed k_t and c_t, respectively. As suggested by Yang et al. [10], such a simple model represents a reasonable solution to model the contact between the wheels and ground when irregularities on the pavement are neglected, providing for a good balance between modeling complexity and the quality of the results. Figure 2 reports a sketch of the tire model.

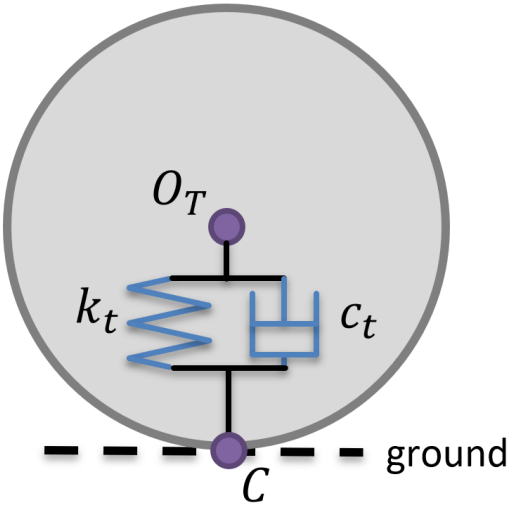

Figure 2. Point-contact tire model.

The vertical force exerted on the tire contact point C, i.e., the third component of the tire force expressed in tire frame $\mathcal{T}$, is

$$f_{C_z}^{\mathcal{T}} = -\left(c_t\dot{\delta}_t + k_t\delta_t\right) \tag{11}$$

where δ_t is the tire deflection and $\dot{\delta}_t$ its time derivative. The force acts parallel to the third unit vector of the tire frame $\boldsymbol{t}_3$ and in the opposite direction.

2.2.2. Shock Absorber Model

An equivalent single-orifice shock absorber model is employed through a nonlinear preloaded spring-damper system [24]. The elastic and damping force can accordingly be expressed as

$$F_{gas} = \frac{p_o A_c}{\left(1 - \frac{A_c}{V_0}\delta_s\right)^{\gamma_{gas}}} \tag{12a}$$

$$F_{oil} = \frac{1}{2}\rho_{oil}\frac{A_c^3}{\left(c_d A_o(\delta_s)\right)^2}|\dot{\delta}_s|\dot{\delta}_s \tag{12b}$$

where δ_s is the absorber stroke, $\dot{\delta}_s$ is its rate, p_0 is the cylinder preload pressure (internal pressure when $\delta_s = 0$), A_c is the cross-section area of the cylinder, V_0 is the shock absorber internal volume when $\delta_s = 0$, γ_{gas} is the gas (air or nitrogen) polytropic coefficient, ρ_{oil} is the oil density, c_d is the orifice discharge coefficient, and A_o is the equivalent orifice cross-section area.

Equation (12a) show that, even for $\delta_s = 0$, the shock absorber exerts an internal force due to the preload pressure p_0, equal to $F_0 = p_0 A_c$. When the force applied at the strut exceeds the preload force, the strut begins to compress.

2.2.3. Ground Contact Detection

Landing simulations require the detection of the instants in which each tire touches the ground or rebounds. The contact condition is formulated similarly to Lei et al. [16].

The position of the contact point for the undeformed tire with respect to the airplane center of gravity $\boldsymbol{r}_{C,G}$ is given by

$$\boldsymbol{r}_{C,G} = \boldsymbol{r}_{C,O_T} + \boldsymbol{r}_{O_T,O_S} + \boldsymbol{r}_{O_S,G}, \tag{13}$$

where $\boldsymbol{r}_{C,O_\mathcal{T}}$ is the position of point C with respect to the wheel center and $\boldsymbol{r}_{O_\mathcal{T},O_\mathcal{S}}$ is the position of the wheel center with respect to the point where the strut is attached to the airplane, while $\boldsymbol{r}_{O_\mathcal{S},G}$ is the position of $O_\mathcal{S}$ with respect the center of gravity G.

Assuming a rigid airplane, the components of $\boldsymbol{r}_{O_\mathcal{T},O_\mathcal{S}}$ and $\boldsymbol{r}_{O_\mathcal{S},G}$ in the body frame are readily obtained from the geometry of the airplane, whereas the position of the contact point C with respect to the wheel center is readily defined in tire coordinates $\mathcal{T}$ as

$$\boldsymbol{r}^{\mathcal{T}}_{C,O_\mathcal{T}} = \begin{Bmatrix} 0 & 0 & r_{t_0} \end{Bmatrix}^T \tag{14}$$

where r_{t_0} is the undeformed tire radius. Notice also that $\boldsymbol{r}^{\mathcal{T}}_{C,O_\mathcal{T}} = \boldsymbol{r}^{\mathcal{N}}_{C,O_\mathcal{T}}$, since the tire and NED frames are parallel.

The components in the NED frame of point C are readily available through

$$\boldsymbol{r}^{\mathcal{N}}_{C,G} = \boldsymbol{r}^{\mathcal{T}}_{C,O_\mathcal{T}} + \boldsymbol{R}^{\mathcal{N}}_{321}\boldsymbol{r}^{\mathcal{B}}_{O_\mathcal{T},O_\mathcal{S}} + \boldsymbol{R}^{\mathcal{N}}_{321}\boldsymbol{r}^{\mathcal{B}}_{O_\mathcal{S},G}, \tag{15}$$

in which tensor $\boldsymbol{R}_{321}$ has been used for transforming the components of $\boldsymbol{r}_{O_\mathcal{T}}$, $O_\mathcal{S}$, and $\boldsymbol{r}_{O_\mathcal{S},G}$ from reference $\mathcal{B}$ to $\mathcal{N}$.

Finally, the distance L between the contact point on the wheel and the ground along the third axis of the NED frame can be easily computed through the following scalar product

$$L = \left(\boldsymbol{r}_{G_0,G} - \boldsymbol{r}_{C,G}\right) \cdot \boldsymbol{n}_3, \tag{16}$$

where $\boldsymbol{r}_{G_0,G} \cdot \boldsymbol{n}_3$ is the altitude of the airplane, which is computed integrating Equation (10).

The tire has touched the ground when L becomes negative. When this condition is triggered, landing gear dynamics start to act.

2.2.4. Ground Contact Forces and Moments

Once the aircraft has touched the ground, the reaction forces on the contact point arise. Each landing gear contact point generates three forces, which are the normal force, acting perpendicularly to the ground, and two in-plane forces due to friction, acting parallel to the ground surface. Associated with the reaction forces, their moments with respect to the aircraft center of gravity are considered as well. Assuming the deformation of the tire is negligible, the expressions of the reaction forces $\boldsymbol{f}_\mathrm{r}$ and moments $\boldsymbol{m}_{\mathrm{r}G}$ expressed in the body frame are

$$\boldsymbol{f}^{\mathcal{B}}_\mathrm{r} = \left(\boldsymbol{R}^{\mathcal{N}}_{321}\right)^T \begin{Bmatrix} -\mu_x \\ -\mu_y(\tau) \\ -1 \end{Bmatrix} \left(c_t\dot{\delta}_t + k_t\delta_t\right) \tag{17a}$$

$$\boldsymbol{m}^{\mathcal{B}}_{\mathrm{r}\,G} = \left(\left(\boldsymbol{R}^{\mathcal{N}}_{321}\right)^T \boldsymbol{r}^{\mathcal{N}}_{C,G}\right) \times \boldsymbol{f}^{\mathcal{B}}_\mathcal{T}, \tag{17b}$$

where μ_x and μ_y are, respectively, the longitudinal and lateral friction coefficients, while τ is the skid angle defined as $\tau = \arctan(v_C/u_C)$, with v_C and u_C being the longitudinal and lateral speed of the tire at the contact point C in the tire frame. The skid angle basically describes how much the wheel drifts with respect to its longitudinal velocity. The dependency of μ_y on the skid angle τ, as reported in [13], is emphasized in Equation (17a).

2.3. Software Implementation

All equations of motion representing aircraft and landing gear dynamics were implemented in Matlab® [25] and integrated with the Runge–Kutta scheme of fourth and fifth orders through the function `ode45`.

In order to avoid numerical issues, the ground contact detection algorithm (Section 2.2.3) is included in the simulation as the `Event` option of the function `ode45`. This option makes it possible to stop the simulation whenever specific events, the ground contact or rebound of a leg in the present case, are detected.

Accordingly, the overall landing simulation is divided into multiple sub-simulations. Anytime a tire gets in contact with the ground or rebounds, the time marching stops and the subsequent sub-simulation starts using the final state vector of the previous sub-simulation as the initial condition. Clearly, when a wheel touches the ground the dynamics of the related tire will be included in the subsequent sub-simulation. Vice versa, when it rebounds, the opposite happens, i.e., the dynamics of the tire is excluded.

2.4. Reference Airplane Definition

A flight mechanics model of a realistic airplane, inspired by the Lockheed Jetstar, has been used for the numerical analyses of this work. The aerodynamic data were extracted from already published NASA reports [26–28], while realistic landing gear properties, including shock absorbers and tires, were defined following design guidelines provided by Roskam [29], Torenbeek [30], and Currey [31]. Finally, real tire data were retrieved from Goodyear's aviation tires catalog [32]. A comprehensive list of the reference aircraft data is provided in Appendix A.

3. Airplane Trim in Non-Null Horizontal Wind Conditions

Null wind conditions are typically assumed in the analysis of the trim of flying systems (see [33] and the references therein). In this work, we extend such treatment to the case of steady wind.

Let us consider the nonlinear equations of motion for a rigid aircraft, as in Equation (2). A trimmed flight is a regime in which the linear and angular velocity vector, viewed in the body frame, $\boldsymbol{v}^{\mathcal{B}}$ and $\boldsymbol{\omega}^{\mathcal{B}}$, are constant for constant controls $\boldsymbol{\delta}$, i.e.,

$$\boldsymbol{\delta} = \overline{\boldsymbol{\delta}} = \text{const.} \;\Rightarrow \boldsymbol{v}^{\mathcal{B}} = \overline{\boldsymbol{v}} = \text{const. and } \boldsymbol{\omega}^{\mathcal{B}} = \overline{\boldsymbol{\omega}} = \text{const.} \tag{18}$$

The trim problem hence consists of finding, if any, the constant vectors $\overline{\boldsymbol{v}}$, $\overline{\boldsymbol{\omega}}$, and $\overline{\boldsymbol{\delta}}$ along with the evolution of the Euler angles $\boldsymbol{e}_{321}(t)$, which are not necessarily constant, which satisfies the nonlinear equations of motion in Equation (2).

Trim analysis for null wind conditions leads to the fact that, in order for trajectories to be trimmed, the airplane angular velocity vector must be either null or constant and parallel to gravity. Consequently, all steady rectilinear flight regimes (e.g., horizontal, climb, or descent) are trimmed, as well as all steady turning flights and helices, with the latter being the most generic trimmed conditions, as noticed by De Marco et al. [33]. For non-null wind conditions, as we will see in the following paragraphs, the set of flight regimes that can be trimmed is narrower.

3.1. Non-Null Wind Condition

Let us now introduce the wind velocity in the NED frame as

$$\boldsymbol{v}_{\mathrm{w}}^{\mathcal{N}} = \left(v_{\mathrm{wOstro}},\, v_{\mathrm{wPonente}},\, v_{\mathrm{wVertical}}\right)^{T}, \tag{19}$$

where v_{wOstro} and v_{wPonente} are the components blowing, respectively, from the south towards the north and from the west towards the east, which represent the *horizontal wind*. The component $v_{\mathrm{wVertical}}$ is the vertical wind, which is positive if "up-down". Moreover, we assume that the wind velocity in the NED frame $\boldsymbol{v}_{\mathrm{w}}^{\mathcal{N}}$ is constant in time and uniform over space.

In order to compute the impact of the wind on the aerodynamic forces and moments, one has to refer to the wind components in the body frame, which can be computed easily through the change of basis as

$$\boldsymbol{v}_{\mathrm{w}}^{\mathcal{B}} = \left(\boldsymbol{R}_{321}^{\mathcal{N}}\right)^{T} \boldsymbol{v}_{\mathrm{w}}^{\mathcal{N}}. \tag{20}$$

The three components of $\boldsymbol{v}_{\mathrm{w}}$ in the body frame are named, respectively, the *tailwind* $v_{\mathrm{W}x}$, which is positive if it is towards the airplane nose, the *crosswind* $v_{\mathrm{W}y}$, which is positive

if it is towards the right side of the airplane, and the *normal wind* v_{W_z}, which is positive if it is towards the airplane down side.

Equations (2b), (7b) and (20) can be combined, and evaluated for null reaction forces and moments, under the hypothesis of the trimmed regime in Equation (18), yielding

$$\begin{aligned}\overline{\omega} \times (M\overline{v}) = f_{\mathrm{a}_{\mathrm{ref}}} + \frac{\partial f_{\mathrm{a}}}{\partial v}\left(\overline{v} - v_{\mathrm{a}_{\mathrm{ref}}}\right) + \frac{\partial f_{\mathrm{a}}}{\partial \omega}(\overline{\omega} - \omega_{\mathrm{ref}}) + \\ + \frac{\partial f_{\mathrm{a}}}{\partial \delta}\left(\overline{\delta} - \delta_{\mathrm{ref}}\right) + \left(R_{321}^{\mathcal{N}}\right)^{T} f_{\mathrm{g}}^{\mathcal{N}} - \frac{\partial f_{\mathrm{a}}}{\partial v}\left(R_{321}^{\mathcal{N}}\right)^{T} v_{\mathrm{w}}^{\mathcal{N}}.\end{aligned} \tag{21a}$$

$$\begin{aligned}\overline{\omega} \times (J_G\overline{\omega}) = m_{\mathrm{a}G\mathrm{ref}} + \frac{\partial m_{\mathrm{a}G}}{\partial v}\left(\overline{v} - v_{\mathrm{a}_{\mathrm{ref}}}\right) + \frac{\partial m_{\mathrm{a}G}}{\partial \omega}(\overline{\omega} - \omega_{\mathrm{ref}}) + \\ + \frac{\partial m_{\mathrm{a}G}}{\partial \delta}\left(\overline{\delta} - \delta_{\mathrm{ref}}\right) - \frac{\partial m_{\mathrm{a}G}}{\partial v}\left(R_{321}^{\mathcal{N}}\right)^{T} v_{\mathrm{w}}^{\mathcal{N}}.\end{aligned} \tag{21b}$$

In Equation (21), the superscript $(\cdot)^{\mathcal{B}}$ has been removed to simplify the notation. Clearly, all terms in Equation (21) but the gravitational ones are constant by definition and, hence, in order to verify them the equality $\left(R_{321}^{\mathcal{N}}\right)^{T} f_{\mathrm{g}}^{\mathcal{N}}$ and the components of the wind in the body frame $\left(R_{321}^{\mathcal{N}}\right)^{T} v_{\mathrm{w}}^{\mathcal{N}}$ must be constant as well. By simply looking at the definitions of the rotation tensor $R_{321}^{\mathcal{N}}$ and the wind velocity $v_{\mathrm{w}}^{\mathcal{N}}$, it is simple to verify that this happens in two cases:

1. For a generic $v_{\mathrm{w}}^{\mathcal{N}}$, all Euler angles are constant, $\dot{\phi} = \dot{\theta} = \dot{\psi} = 0$;
2. For a pure vertical wind, i.e., $v_{\mathrm{w}} || n_3$, roll and pitch angles are constant, $\dot{\phi} = \dot{\theta} = 0$.

As a first remark, notice that the conditions in the second case, associated with a pure vertical wind, $\dot{\phi} = \dot{\theta} = 0$, are the same as the usual trim problem for null wind conditions. This implies that the possible trim conditions associated with pure upward or downward wind are identical to the usual case with null wind. A notable flight trajectory that satisfies the trim equation, Equation (21), for pure vertical upward wind is the ascending helix, which is exploited by gliders to gain height thanks to vertical wind flow.

However, the case with a generic wind, including horizontal wind components, i.e., cross- and tailwind, admits only rectilinear flights. This fact is simple to demonstrate by noticing that constant Euler angles ($\dot{\phi} = \dot{\theta} = \dot{\psi} = 0$) are needed to have a constant rotation tensor $R_{321}^{\mathcal{N}}$ and hence a constant product $\left(R_{321}^{\mathcal{N}}\right)^{T} v_{\mathrm{w}}^{\mathcal{N}}$ in Equation (21b). Looking back to the kinematic relationship in Equation (9), it can be immediately noticed that the conditions $\dot{\phi} = \dot{\theta} = \dot{\psi} = 0$ imply necessarily a null angular velocity ω.

In this case, which is of interest for this work, the trim equations in Equation (21) reduce to the straightforward equilibrium among aerodynamic and gravitational forces and moments.

3.2. Trim Problem Solution Determination for Non-Null Horizontal Wind

The nonlinear trim problem solution can be found by looking for the set of linear and angular velocities, control inputs, and Euler angles that satisfy Equation (21). If horizontal wind components are considered, as demonstrated in Section 3.1, this solution exists only if $\omega = \mathbf{0}$ and there are constant Euler angles. Consequently, the array of the problem unknowns consists of 10 elements and is defined as

$$x_{\mathrm{trim}} = \left(\overline{v}^{T}, \overline{\delta}^{T}, \overline{e}_{321}^{T}\right)^{T}, \tag{22}$$

where $\overline{e}_{321}$ is the vector with the constant Euler angles.

The nonlinear trim problem can be formalized as

$$\boldsymbol{f}_{\mathrm{a}_{\mathrm{ref}}} + \frac{\partial \boldsymbol{f}_{\mathrm{a}}}{\partial \boldsymbol{v}}\left(\overline{\boldsymbol{v}} - \boldsymbol{v}_{\mathrm{a}_{\mathrm{ref}}}\right) + \frac{\partial \boldsymbol{f}_{\mathrm{a}}}{\partial \boldsymbol{\delta}}\left(\overline{\boldsymbol{\delta}} - \boldsymbol{\delta}_{\mathrm{ref}}\right) + \left(\boldsymbol{R}_{321}^{\mathcal{N}}\right)^{T} \boldsymbol{f}_{\mathrm{g}}^{\mathcal{N}} - \frac{\partial \boldsymbol{f}_{\mathrm{a}}}{\partial \boldsymbol{v}}\left(\boldsymbol{R}_{321}^{\mathcal{N}}\right)^{T} \boldsymbol{v}_{\mathrm{w}}^{\mathcal{N}} = 0 \tag{23a}$$

$$\boldsymbol{m}_{\mathrm{a}G_{\mathrm{ref}}} + \frac{\partial \boldsymbol{m}_{\mathrm{a}G}}{\partial \boldsymbol{v}}\left(\overline{\boldsymbol{v}} - \boldsymbol{v}_{\mathrm{a}_{\mathrm{ref}}}\right) + \frac{\partial \boldsymbol{m}_{\mathrm{a}G}}{\partial \boldsymbol{\delta}}\left(\overline{\boldsymbol{\delta}} - \boldsymbol{\delta}_{\mathrm{ref}}\right) - \frac{\partial \boldsymbol{m}_{\mathrm{a}G}}{\partial \boldsymbol{v}}\left(\boldsymbol{R}_{321}^{\mathcal{N}}\right)^{T} \boldsymbol{v}_{\mathrm{w}}^{\mathcal{N}} = 0 \tag{23b}$$

$$\boldsymbol{R}_{321}\overline{\boldsymbol{v}} - \overline{\boldsymbol{v}}^{\mathcal{N}} = 0 \tag{23c}$$

$$p(\beta, \delta_A, \delta_R, \phi, \psi) = 0. \tag{23d}$$

Along with the equilibrium of forces and moments in Equations (23a) and (23b), Equation (23c) is considered to impose a specific trimmed rectilinear trajectory through a specific value of $\overline{\boldsymbol{v}}^{\mathcal{N}}$. In landing, for example, the velocity in the NED frame is dictated by the airplane approach velocity and the glide slope of the trajectory. Finally, Equation (23d) is the classical *piloting condition* and refers to the choices that the pilot follows during the trimmed regime in terms of the variables of the lateral–direction plane. The piloting condition is formulated by fixing one among the sideslip angle β, the aileron deflection δ_A, the rudder deflection δ_R, the roll angle ϕ, or the heading angle ψ to a predefined value. Dealing with landing with horizontal wind, the piloting condition can be set so as to specify a desired landing technique, such as the following:

- $\delta_R = 0$: fly the aircraft without deflecting the rudder;
- $\beta = 0$ or $(\boldsymbol{v} - \boldsymbol{v}_{\mathrm{w}}) \cdot \boldsymbol{b}_2 = 0$: fly the aircraft keeping zero sideslip angle (crabbed flight);
- $\psi - \chi_{\mathrm{RNW}} = 0$: fly the aircraft aligning the heading to ground track orientation χ_{RNW} (steady sideslipped flight).

The conditions defined in the last two bullet points are commonly used during crosswind approaches and landings and, hence, are particularly relevant to this work.

System (23) represents a set of 10 equations in 10 unknowns, which can be solved by a standard nonlinear solver.

4. Landing Optimization for Minimum Tire Wear

During a crosswind landing, lateral friction forces arise on tires at touchdown due to sliding. These forces are the cause of significant wear. Minimizing tire wear due to sliding would lead to a potential extension of tire life, positively impacting the aircraft operations economy. In this work, a preliminary study of a simple maneuver aimed at minimizing tire wear during crosswind landings is carried out. To achieve this goal, first have to describe how one can manage the landing maneuver in crosswind conditions by exploiting the mathematical tools developed in Sections 2 and 3. This specific task is addressed in Section 4.1. Then, it is necessary to define a procedure to evaluate the tire wear from the outputs of the landing simulations and, finally, define the optimization strategy. These two tasks are, respectively, considered in Sections 4.2 and 4.3.

4.1. Crosswind Landing Maneuver

Crosswind landings (and landings in a more general sense) are highly dynamic maneuvers, in which pilots apply corrections in order to maintain control of the aircraft.

As different landing techniques are typically employed in real life, in this work we focus on a simplified maneuver that is a derivation of what is called the "wings-low" or "sideslipped" approach [34]. Starting from a crabbed flight condition (null sideslip), shortly before the flare the aircraft moves to a nonsymmetric flight condition with a non-null sideslip. The sideslip angle is maintained at a constant by applying upwind aileron and downwind rudder deflections, achieving a crossed-control condition, in which the aircraft is flying aligned to the runway and maintains its heading oriented along the desired track. Such a condition is clearly reached in a banked flight condition, with the aircraft banked in the upwind direction. The lift is then adjusted by means of the pitch control. This flight condition is maintained till touchdown and the aircraft touches the ground with the upwind wheel first. The maneuver profile is shown in Figure 3.

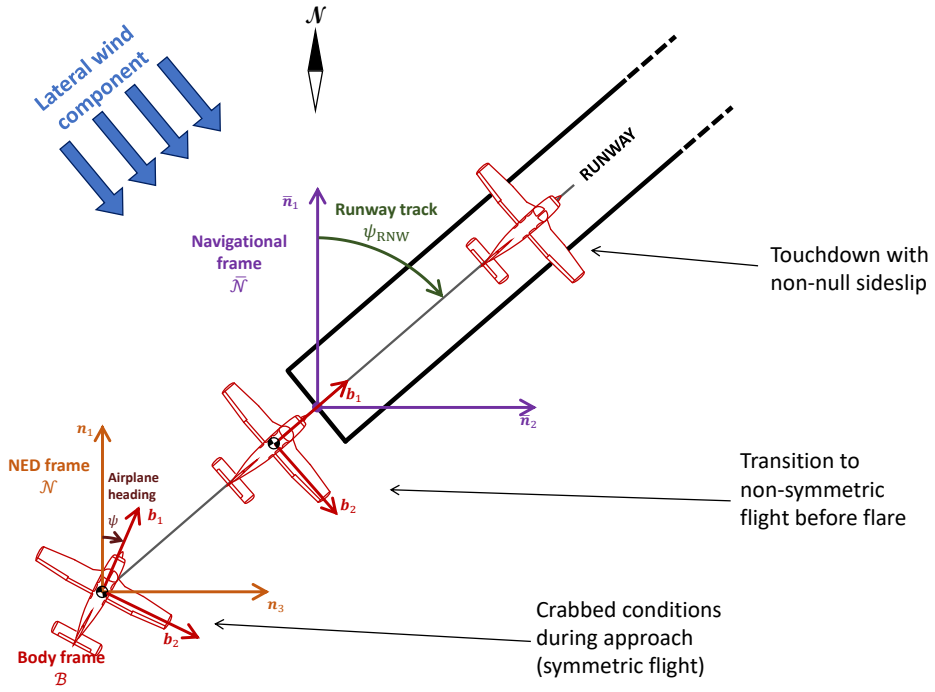

Figure 3. Sideslipped (wings-low) crosswind approach.

In order to simplify the treatment, we assume also that the flare is performed sufficiently in advance, achieving a trimmed flight condition before touchdown. Consequently, the simulation of the landing maneuver can start shortly before touchdown from an initial condition in which the aircraft is flying at a constant rate of descent, i.e., with a glide path angle γ lower than the one of the approach phase, $\gamma < 3\,[\text{deg}]$, with the heading angle equal to the runway track angle $\psi = \chi_{\text{RNW}}$. This condition leads the upwind landing gear leg to make contact with the ground before the downwind one. The trim airspeed may be lower than the approach speed to simulate the speed decrease during the flare. At touchdown, the throttle is set to zero and the elevator control is left at the trimmed position.

When the aircraft touches the ground with both wheels, the aileron and rudder surfaces are moved in order to control the aircraft during the landing ground roll. Typically, the ailerons are displaced in the upwind direction (raising the upwind aileron) during the ground run to counteract the crosswind-induced rolling moment, while the rudder is used for minimizing the lateral deviation.

Simulation of a Landing Maneuver in Crosswind Condition

A simple simulation of a landing maneuver considering a crosswind is here reported to demonstrate the capabilities of the tool developed in this work.

The reference airplane is trimmed, through the procedure explained in Section 3, in the following conditions:

- Airspeed: TAS $= 54.44 \frac{\text{m}}{\text{s}}$;
- Initial height: $z_{\text{G}}^{\mathcal{N}} = -2.5\text{m}$;
- Glide path angle: $\gamma = -0.5^{\text{o}}$;
- Track angle: $\chi = 0^{\text{o}}$;
- Wind direction/wind speed: $090^{\text{o}}/5 \frac{\text{m}}{\text{s}}$.

Notice that, given the previous landing conditions, the wind is blowing exactly from the right side of the aircraft.

The flight variables resulting from the trim solution are then used as the initial condition for landing simulation. To simplify the example, after the touchdown the controls remain fixed at the initial position.

Figure 4 shows the results of this simulation in terms of the most important flight dynamics variables.

Before the aircraft touches the ground with one or more legs, it is stabilized in a wings-low trimmed flight condition, with lateral crossed controls, as shown in Figure 4f, in which both aileron and rudder deflections are positive (i.e., the right wing aileron is raised and the rudder is displaced to the left). The roll angle is positive (i.e., the right wing is lowered) and the heading angle is equal to the track angle (see Figure 4d,e). Given this attitude of the aircraft, the first wheel to touch is the right main gear one at about 0.6 s, followed shortly by the left main gear one at about 0.9 s and by the nose gear one at about 2.4 s (see Figure 4i–k).

After the first contact with the ground, the aircraft rotates about the landing gear contact point (right main gear leg), reducing the roll angle (see Figure 4d), and the aircraft significantly deviates from the straight trajectory (see Figure 4h) as a result of the sustained application of the controls in their trimmed position.

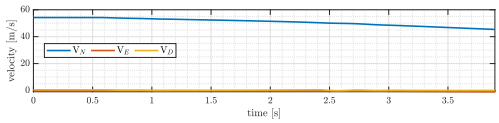

(**a**) Linear velocity components - NED frame

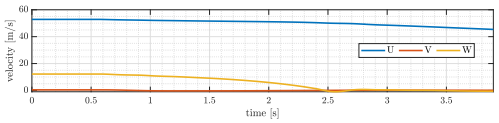

(**b**) Linear velocity components - body frame

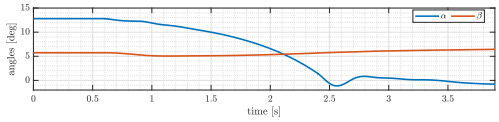

(**c**) Aerodynamic angles

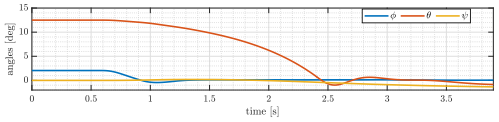

(**d**) Euler angles

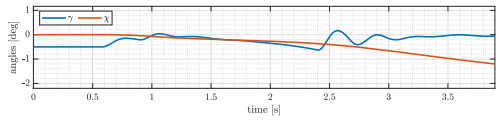

(**e**) Trajectory angles

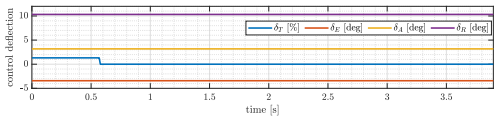

(**f**) Controls

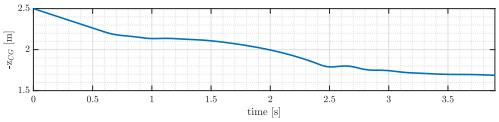

(**g**) CG vertical trajectory - NED frame

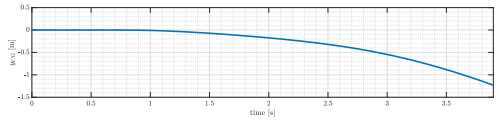

(**h**) CG lateral trajectory - NED frame

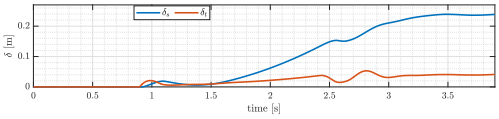

(**i**) Left main gear strut and tire deflection

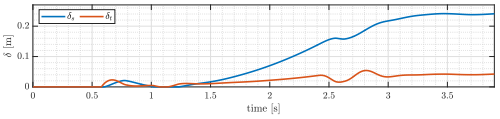

(**j**) Right main gear strut and tire deflection

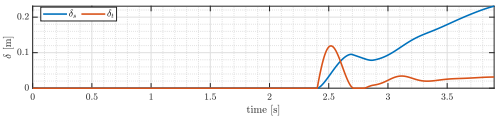

(**k**) Nose gear strut and tire deflection

Figure 4. Example of crosswind landing—$\gamma = -0.1^o$, TAS = 54.44 $\frac{\text{m}}{\text{s}}$, wind direction/wind speed: $090^o/5\frac{\text{m}}{\text{s}}$ (crosswind $v_{\text{W}y} = -5\,\frac{\text{m}}{\text{s}}$).

4.2. Archard Wear Model

With the goal of finding the optimal aileron and rudder control settings to achieve minimal wear of tires, in this section we will introduce a simple estimation of tire wear, according to the Archard model [20].

Wear is the mechanical (or chemical) degradation of surfaces and is a central aspect in estimating the service life of any technical system, [35]. When dealing with tires, the main sources of wear are abrasion and fatigue, as reported by van der Veen [36].

Archard focused on the studies of Reye [19], which stated that the volume rate of worn material is proportional to power dissipation due to friction forces. Consequently, the volume of abraded material is proportional to the work performed by sliding friction forces. Consequently, according to the Archard model, the worn material volume ΔV can be expressed as

$$\Delta V = k_a \frac{W_f}{H} \tag{24}$$

where W_f corresponds to the work of the dissipation forces, k_a is the abrasion factor, and H is the hardness of the worn material. The abrasion factor k_a describes how intense the wearing is. This factor is dimensionless, and its magnitude varies between 10^{-9} (light wear) and 10^{-3} (intense wear). The hardness H is defined as a measure of the resistance to localized plastic deformation induced by abrasion. This factor is commonly measured in the "Shore-Hardness" but may be easily referred to SI units by means of conversion tables. The order of magnitude of rubber tire hardness is $1.6 \cdot 10^6 \frac{\mathrm{N}}{\mathrm{m}^2}$.

Finally, considering a tire sliding along its longitudinal and lateral direction, the Archard relation can be finally expressed as follows [37]:

$$\Delta V = k_a \frac{W_x + W_y}{H} \tag{25}$$

where W_x and W_y are the work of longitudinal and lateral dissipation forces, respectively.

The work of the dissipation forces may be expressed in the following integral

$$W_f = \int_{t_{TD}}^{t_{end}} \boldsymbol{f}_f \cdot \boldsymbol{v}_{\mathcal{T}}\, dt \tag{26}$$

where $\boldsymbol{f}_f$ is friction force and $\boldsymbol{v}_C$ is the tire velocity referred to the contact point. The integral is carried out between the touchdown time t_{TD} and a suitable end time, t_{end}.

Equation (26) can be expressed in terms of the horizontal components of the dissipative forces, recalling the fact that friction forces are associated with the normal forces through the friction coefficient, as

$$W_f = \int_{t_{TD}}^{t_{end}} \left(|\mu_x f_{C_z}^{\mathcal{T}} v_{C_x}^{\mathcal{T}}| + |\mu_y(\tau) f_{C_z}^{\mathcal{T}} v_{C_y}^{\mathcal{T}}| \right) dt \tag{27}$$

where $f_{C_z}^{\mathcal{T}}$ is the vertical reaction force, as defined in Equation (11), μ_x and μ_y are, respectively, the longitudinal and lateral tire friction coefficients, whereas $v_{C_x}^{\mathcal{T}}$ and $v_{C_y}^{\mathcal{T}}$ are, respectively, the longitudinal and lateral velocity components of the tire, expressed in tire axes.

The work dissipated by the tires of the landing gear is then defined as the sum of the contributions of each tire:

$$W_f = \int_{t_{TD}}^{t_{end}} \sum_{i=1}^{n_T} \left(|\mu_x f_{C_z}^{\mathcal{T}} v_{C_x}^{\mathcal{T}}| + |\mu_y(\tau) f_{C_z}^{\mathcal{T}} v_{C_y}^{\mathcal{T}}| \right)_i dt \tag{28}$$

where $i = 1, \ldots, n_T$ is the index of the tire and n_T is the total number of tires of the landing gear. In the present tricycle landing gear model, each leg is equipped with an equivalent tire; hence, $n_T = 3$.

4.3. Optimal Landing in Crosswind Conditions for Minimum Tire Wear

During landing, the main friction contributions acting on tires within the first instants after touchdown are due to wheel spin and tire sliding. Considering only the transverse direction, which is more relevant in the case of crosswind landing, the work of the lateral friction forces W_{f_y} results in

$$W_{f_y} = \int_{t_{TD}}^{t_{end}} \sum_{i=1}^{3} \left(\left| \mu_y(\tau) f_{C_z}^{\mathcal{T}} v_{C_y}^{\mathcal{T}} \right| \right)_i dt. \tag{29}$$

W_{f_y} can be then used as a cost function to be minimized in order to define the optimal landing maneuver in crosswind conditions. Notice that all variables in Equation (29), i.e., $f_{C_z}^{\mathcal{T}}$ and $v_{C_y}^{\mathcal{T}}$, are easily evaluated within the simulation environment as described in Section 2. In fact, $f_{C_z}^{\mathcal{T}}$ is given by Equation (11), whereas the lateral velocity of the tire contact point $v_{C_y}^{\mathcal{T}}$ is the second component of the contact point velocity vector $\boldsymbol{v}_C = \boldsymbol{v} + \omega \times \boldsymbol{r}_{C,G}$, expressed in the tire frame $\mathcal{T}$, being $\boldsymbol{r}_{C,G}$ the position vector of the contact point C with respect to the center of gravity G.

The landing maneuver, which minimizes the tire wear in crosswind direction, is then found by solving the following optimal problem:

$$\min_{\boldsymbol{q}} W_{f_y}(\boldsymbol{q}) \text{ such that } \boldsymbol{q}_{\mathrm{L}} \leq \boldsymbol{q} \leq \boldsymbol{q}_{\mathrm{U}} \tag{30}$$

where the $\boldsymbol{q}$ is the array of the optimization parameters to be defined, whereas $\boldsymbol{q}_{\mathrm{L}}$ and $\boldsymbol{q}_{\mathrm{U}}$ are the related upper and lower limits. In this work, the solution of Problem (30) is found through an SQP algorithm implemented in the Matlab function `»fmincon` [38].

Within array $\boldsymbol{q}$, one may consider all variables affecting the landing maneuver, such as the control inputs and/or the trim conditions before touchdown. In Section 5, the different choices for $\boldsymbol{q}$ will be detailed.

5. Results

5.1. Preliminary Parametric Study

In order to better understand how tire wear is influenced by the control deflections that a pilot imposes immediately after both legs of the main landing gear touch the ground, a parametric analysis has been performed to map the tire wear W_{f_y} as a function of such aileron and rudder deflections, which are indicated, respectively, with δ_A and δ_R. Although the elevator input may also impact tire wear, it was not included in the analysis.

At first, a standard landing in calm air has been considered. In this case, it is expected that the minimum of the wear is associated with null control deflections. Then, a landing with a crosswind of 5 m/s coming from the right side of the airplane is analyzed in order to study its influence combined with the effects of controls. Both cases consider touchdown airspeed equal to 61.25 m/s and glide path angle $\gamma = -0.5$ deg.

After the instant in which all legs touch the ground, the simulator keeps constant δ_A and δ_R till the end of the simulation, which is imposed 3 s after the contact between the main gear and the ground.

Figure 5 shows the contour plots of the tire wear as a function of the control δ_A and δ_R for a symmetric landing without wind (left plot) and with a crosswind equal to 5 m/s (right plot). In both plots, a red dot indicates the controls at the trim condition during the airborne phase, whereas the green triangle indicates the minimum of the wear W_{f_y}.

From Figure 5a, it is evident that the cost function has a symmetrical behavior with respect to the point $(\delta_A, \delta_R) = (0, 0)$, which is also identifiable as the minimum. In fact, as the analysis occurs starting from a symmetrical landing condition in which both the aileron and rudder are not deflected, the ground contact is symmetric and the ground run

occurs without side deviation: the minimum tire wear due to side friction is unsurprisingly expected at $\delta_A = 0\,\text{deg}$ and $\delta_R = 0\,\text{deg}$.

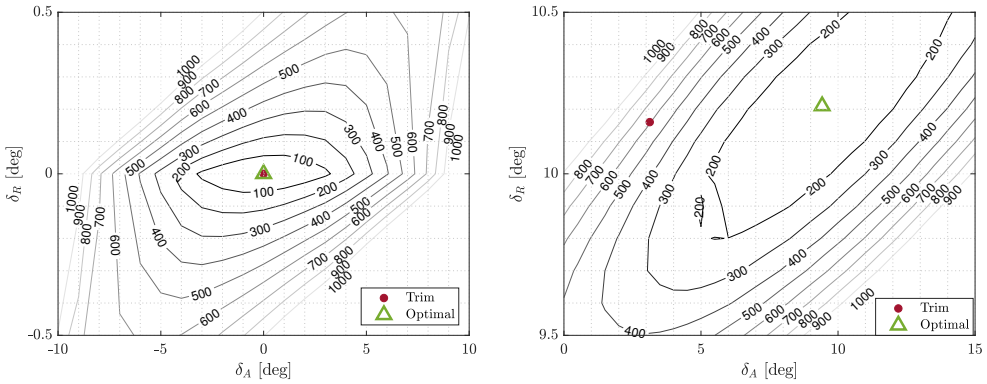

(**a**) (**b**)

Figure 5. Cost function mapping. Left plot: null crosswind; right plot: crosswind $v_{\text{W}y} = -5\,\frac{\text{m}}{\text{s}}$. (**a**) Cost function contour: null crosswind. (**b**) Cost function contour: crosswind 5 m/s.

An interesting, but again unsurprising, consideration may be derived by looking at the magnitude of the impact of flight controls on the cost function trend. If we consider the minimum point as a reference (Figure 5a), it is clear that an aileron deflection after touchdown has a less intense effect on the cost function than a rudder one: aileron deflection of 4 degrees causes the same effect that is obtained by applying a rudder deflection of 0.1 degrees. Hence, the parameter that is most likely going to influence the wear minimization is the rudder deflection.

Consider now the map related to the landing in crosswind conditions. Before analyzing the cost function contour in Figure 5b, some preliminary considerations on the expected output can be investigated. After touchdown with a lateral wind from the right side, a pilot would deflect upward the upwind aileron, in order to compensate for the wind-induced rolling moment while setting the rudder to keep the airplane on the ground track.

The contour plot of the tire wear, shown in Figure 5b, exhibits a trend consistent with that obtained without crosswind, with the minimum shifted in a region where both the ailerons and rudder are positively deflected, i.e., $\delta_A, \delta_R > 0$, confirming that crossed control settings after the touchdown are associated with the optimal performance. Quite interestingly, the expected optimal control settings are partially coherent with the pilot inputs normally applied after touchdown: with respect to the trimmed control settings, ailerons are positively deflected, whereas the rudder is kept nearly at the trimmed setting, suggesting that the lateral deviation of the trajectory after touchdown may be significant.

5.2. Optimal Landing in Crosswind Conditions for Different Glide Angles and Approach Velocities

Given the first insight on the cost function behavior, the optimization algorithm is now applied to find the optimal control setting that leads to tire wear minimization for a wide variety of initial conditions, given a fixed crosswind speed equal to 5 m/s. The test conditions are defined in terms of the glide path angle γ and airspeed at touchdown.

Recalling the expression of the general optimization problem, Equation (30), the optimization variables are the aileron and rudder deflections after the touchdown of both tires of the main landing gear, $\boldsymbol{q} = (\delta_{\text{A}}, \delta_{\text{R}})$, whereas the bounds of both optimization variables are set to $\pm 20\,\text{deg}$. Finally, to ensure that the solver converges to the absolute minimum, the optimization is repeated several times starting from randomly chosen initial guesses within the bounds of the optimization variables.

The optimization results are reported in Table 1. The first two columns of Table 1 show, respectively, the selected values of the approach velocity and the glide path angle. The third, fourth, and fifth columns report the most significant flight variables at the trim before touchdown, i.e., the sideslip angle β_{trim} and the lateral–directional controls $\delta_{\text{A}_{\text{trim}}}$ and $\delta_{\text{R}_{\text{trim}}}$.

In accordance with the "wings-low" landing approach (see Figure 3), the sideslip angle β_{trim} results are uniquely determined by the values of the approach speed $||v||$ and crosswind v_{Wy}, as $\beta_{\text{trim}} = \arcsin\left(v_{Wy}/||v||\right)$.

The last three columns represent, respectively, the optimal variables $\delta_{A_{\text{opt}}}$ and $\delta_{R_{\text{opt}}}$ associated with the minimum cost function, i.e., the work of the dissipative forces W_{f_y} in the last colum.

Table 1. Optimization test conditions and results. Crosswind $v_{Wy} = -5\ \frac{\text{m}}{\text{s}}$. Variable $U_0 = 68.05$, as defined in Appendix A.

$\|\|v\|\|$	γ [deg]	β_{trim} [deg]	$\delta_{A_{\text{trim}}}$ [deg]	$\delta_{R_{\text{trim}}}$ [deg]	$\delta_{A_{\text{opt}}}$ [deg]	$\delta_{R_{\text{opt}}}$ [deg]	W_{f_y} [J]
$0.8\,U_0$	-0.1	5.73	3.18	10.32	8.92	9.80	54.30
	-0.5	5.73	3.18	10.32	9.86	9.92	82.85
	-1.0	5.73	3.18	10.32	9.19	10.08	241.99
$0.9\,U_0$	-0.1	5.00	3.13	10.16	8.59	10.00	71.65
	-0.5	5.00	3.13	10.16	9.42	10.21	103.34
	-1.0	5.00	3.13	10.16	10.89	10.55	265.85
U_0	-0.1	4.43	3.08	10.00	10.84	10.35	89.43
	-0.5	4.43	3.08	10.00	12.31	10.72	111.69
	-1.0	4.43	3.08	10.00	15.93	11.43	247.05

From Table 1, one can easily observe that conditions with lower tire wear are associated with a lower landing airspeed and lower glide path. This is not unexpected, since tire wear depends on friction force, which in turn depends on the vertical reaction to which the tires are subject. landing with a lower vertical speed entails a gradual load of the tire during the most critical phase, that is, the touchdown, in which the tire is sliding in its transverse direction because of the nonsymmetrical contact condition.

It is also interesting to notice that within the lower airspeed case the difference in the work of friction forces between the lowest and the highest glide path angles is extremely marked: reducing the glide path angle from $\gamma = -1.0^{\text{o}}$ to $\gamma = -0.1^{\text{o}}$ allowed a work dissipation reduction of about 77%. A similar trend is recognized for the other cases with higher approach velocities.

Let us now consider the optimal control variables. As noticed during the preliminary parametric study in Section 5.1, after touchdown the aileron is displaced in the upwind direction, whereas the rudder settles near the trimmed one. This trend also stays the same for different initial conditions. However, it is interesting to notice that the magnitude of the deflections increases as the glide path angles become more pronounced. The most critical cases appear to be those associated with the highest approach speed.

5.3. Optimization Including Sideslip Angle at Trim

So far, the initial trim condition was set considering the piloting technique, which enabled the aircraft to fly with runway heading (i.e., without being misaligned with respect to the runway, $\psi = \chi_{\text{RNW}}$). This means that, given the airspeed value and crosswind speed, the sideslip angle at touchdown was imposed, with flight controls and attitude angles set to maintain the trim condition.

With the aim of understanding whether a different touchdown condition can improve tire wear, the sideslip angle at trim is now included in the array of the optimization variables. In practice, the aircraft can be allowed to touch the ground with a small misalignment angle and, hence, the constraint that $\psi = \chi_{\text{RNW}}$ before touchdown, which was used in the previous analyses, is now neglected. Accordingly, the array of optimization variables is now as follows:

$$\boldsymbol{q} = (\delta_{\text{A}}, \delta_{\text{R}}, \beta_{\text{trim}}) \tag{31}$$

The optimization problem is then formulated as the one of finding the sideslip angle at trim β_{trim} and the control settings after touchdown δ_A and δ_R associated with the minimum tire wear.

The aircraft is flown towards the runway, which is the track angle χ fixed, without being necessarily aligned to the runway heading. In this scenario, the trim piloting condition, Equation (23d), is set as follows:

$$\beta = \beta_{\text{trim}} \Rightarrow \beta_{\text{trim}} - \arcsin\left(\frac{(\boldsymbol{v} - \boldsymbol{v}_{\text{W}}) \cdot \boldsymbol{b}_2}{||\boldsymbol{v}||}\right) = 0, \tag{32}$$

where β_{trim} is now one of the optimization variables.

Now that the minimization algorithm also considers a variable that is computed throughout the trim process, the trim algorithm itself becomes part of the cost function computation. At each evaluation of the W_{f_y}, for a given set of the optimization variables, first, the algorithm computes the initial conditions through the trim analysis (see Section 3.2), then the landing is simulated and the work of the friction forces is computed.

The same optimization tests of Table 1 have been considered, so as to allow for a comparison between the two different landing strategies. To ease the convergence of the optimization, the bounds of the optimization variables were reduced to $\delta_{\text{A}} \in [0, 20]$deg, $\delta_{\text{R}} \in [0, 20]$deg, and $\beta_{\text{trim}} \in [0, 10]$deg. In particular, the lower limit for the sideslip angle has been chosen considering that landing with a null sideslip angle corresponds to touching the ground without de-crabbing during the flare. This technique is not expected to be optimal, because the tires would immediately experience a strong side force, as a result of a consistent side velocity component. Clearly, a negative lower bound would have implied an even worse scenario. Notice that this assumption works only in the case of crosswind coming from the right side of the airplane (e.g., $v_{\text{W}y} < 0$ as in the present analysis). If the wind were to blow in the opposite direction, one would modify the upper bounds of the optimization variables instead of the lower ones.

Table 2 summarizes the conditions and the obtained results of the optimal landing including the sideslip angle at trim within the optimization variables. Now, the third column refers to the sideslip angle at trim $\beta_{\text{trim}_{\text{opt}}}$ found by the optimization algorithm, whereas the fourth and the fifth columns refer to the trim control settings $\delta_{\text{A}_{\text{trim}}}$ and $\delta_{\text{R}_{\text{trim}}}$ associated with $\beta_{\text{trim}_{\text{opt}}}$. The last column shows the percentage reduction in the tire wear with respect to the case with null sideslip angle at trim reported in Table 1.

Table 2. Optimization test conditions and results including sideslip angle within the optimization variables. Crosswind $v_{\text{W}y} = -5\,\frac{\text{m}}{\text{s}}$. Variable $U_0 = 68.05$ as defined in Appendix A.

$\|\|v\|\|$	γ [deg]	$\beta_{\text{trim}_{\text{opt}}}$ [deg]	$\delta_{\text{A}_{\text{trim}}}$ [deg]	$\delta_{\text{R}_{\text{trim}}}$ [deg]	$\delta_{\text{A}_{\text{opt}}}$ [deg]	$\delta_{\text{R}_{\text{opt}}}$ [deg]	W_{f_y} [J]	Reduction with respect to the Results of Table 1
$0.8\,U_0$	-0.1	5.81	3.22	10.47	8.76	9.84	48.22	11%
	-0.5	5.75	3.19	10.37	9.83	9.93	82.10	0.9%
	-1.0	5.62	3.13	10.14	9.22	10.01	229.35	5%
$0.9\,U_0$	-0.1	5.15	3.22	10.14	8.39	10.09	49.31	31%
	-0.5	5.08	3.18	10.30	9.38	10.25	97.82	5%
	-1.0	4.92	3.08	9.99	10.95	10.49	254.66	4%
U_0	-0.1	4.63	3.22	10.44	9.59	10.38	49.161	45%
	-0.5	4.44	3.08	10.01	12.24	10.71	110.4	1%
	-1.0	4.34	3.01	9.78	15.97	11.35	230.10	7%

Comparing Tables 1 and 2, one can immediately notice that, in all cases, landing with some misalignment with respect to the runway leads to significantly lower tire wear. The entity of the reduction is highly variable and may be up to 45%. Focusing on the realistic case with the lowest landing velocity and most gentle glide path, i.e., $||v|| = 0.8\,U_0$ and

$\gamma = -0.1$ deg, the value of the work of the friction forces is equal to 54.3 J for fixed sideslip and to 48.2 J for optimized sideslip, with a reduction of about 11%.

Moreover, looking at the initial conditions, it is possible to verify that the difference between the optimized sideslip angle and the fixed one is limited, i.e., about 0.1 deg, which is reflected in slightly different trim control settings in terms of both aileron and rudder deflections.

To understand where this difference might have originated, the work dissipation time histories for both cases are plotted in Figure 6, which shows the contribution to the work of the friction forces, i.e., the function to be integrated in Equation (29), as a function of time, for both approaches, i.e., without optimizing the sideslip at trim ($\psi = \chi_{\mathrm{RNW}}$) and including this variable within the optimization parameters ($\psi = \chi_{\mathrm{RNW}}$). The bottom figure shows the overall tire wear displaying the function to be integrated in Equation (29). Additionally, in the top figures, the separated contributions of the left and right main gear are reported: each subplot details the trend of the lateral force (first row), the lateral velocity (second row), and the resulting contribution to the work of the friction forces (third row).

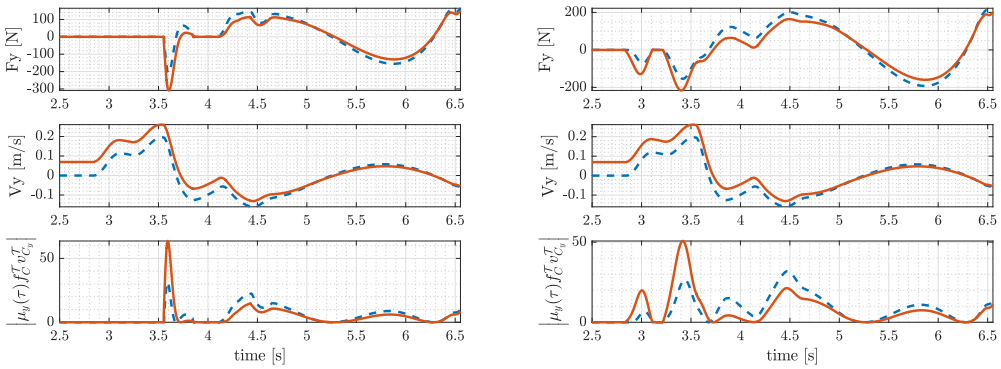

(**a**) Left main gear

(**b**) Right main gear

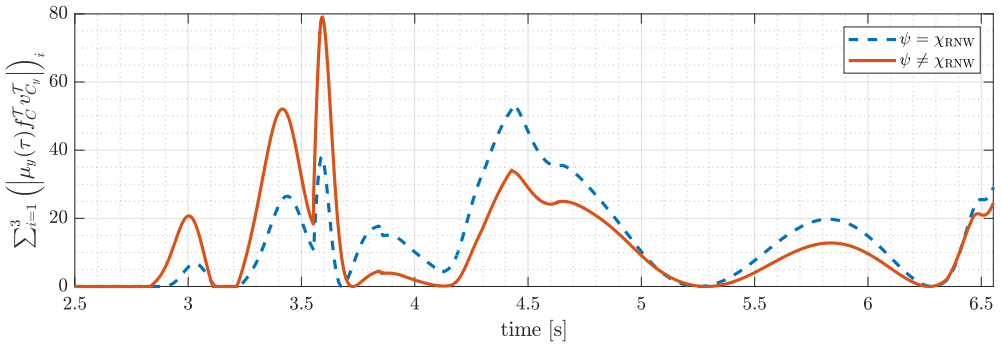

(**c**) Overall contribution to the tire wear

Figure 6. Comparison between two optimal landing approaches at $||v|| = 0.8\,U_0$ and $\gamma = -0.1$ deg. Blue dashed line ($\psi = \chi_{\mathrm{RNW}}$): optimization without sideslip at trim as in Table 1; red solid line ($\psi \neq \chi_{\mathrm{RNW}}$): optimization including sideslip at trim within the optimization variable as in Table 2. Top-left plot: contribution of the left main gear; top-right plot: contribution of the right main gear; bottom plot: overall tire wear. Top plots display in the three subplots the lateral force in the contact point C F_y, the lateral velocity of the contact point C V_y, and the dissipation power associated with the lateral forces $|\mu_y\, f_{C_z}^{\mathcal{T}}\, f_{C_y}^{\mathcal{T}}|$ (see Equation (26)).

As already mentioned, the work dissipation exhibits a highly irregular behavior, with peaks and discontinuities due to the complex ground–tire interaction and the contribution given by three landing gear legs, which touch the runway at different instants. Hence, finding a physical interpretation of the obtained results is complex. Nonetheless, some useful considerations can be made.

Preliminarily, given the landing and wind conditions considered in this example, it is important to notice that, with a roll angle at trim positive ($\phi > 0$), the aircraft touches the ground with the right leg first at second 2.8, followed by the left one at second 3.5, and, finally, by the nose one. The detailed plot of the contact between the nose gear and the terrain is not shown in Figure 6 as it occurs at second 6.5 circa and does not significantly affect the overall tire wear.

We may now consider the top plots of Figure 6, which allow for a comparison of the cost function contributions of the left and right main gear for the two cases. As a first observation, notice that the airplane initially undergoes a lateral displacement to the right (positive lateral speed V_y) when only the right leg is in contact with the ground (between seconds 2.8 and 3.5). Then, after the second leg touches the ground (after second 3.5) a lateral overshoot to the left is experienced by the system (negative lateral speed V_y). This trend is common to both landing approaches. Focusing on the first seconds of the touchdown (between seconds 2.8 and 3.5), it is evident that the peak of the tire wear for the right gear (top-right plot, third subplot) is clearly higher if the airplane heading is misaligned with respect to the runway, $\psi \neq \chi_{\mathrm{RNW}}$. However, when the second leg also comes into contact with the terrain (after second 3.5), the combined effect of the airplane motion and the initial misalignment with respect to the runway leads to a lower lateral overshoot and lower friction forces. As a result, the overall tire wear, which corresponds to the integral of the curves displayed at the bottom plot, is lower if a mild misalignment of the airplane with respect to the runway ($\psi \neq \chi_{\mathrm{RNW}}$) is considered immediately before the airplane touches the ground. This justifies the difference in the performance obtained for the two landing approaches studied in this work and reported in Tables 1 and 2. Similar considerations, not shown here for the sake of brevity, can be derived from other tests considered in this work.

6. Conclusions

This work deals with the optimization of the landing technique in crosswind conditions for minimum tire wear.

In order to achieve this goal, first, a simulator capable of handling the landing maneuver in crosswind conditions was developed. The simulator considers a three-dimensional model of the coupled airplane-landing gear system.

The airplane is modeled as a rigid body in a three-dimensional domain, subject to gravitational, propulsive, aerodynamic, and reaction forces and moments. The aerodynamics, linearized about a suitable condition and rendered through the classical stability and control derivatives, consider also the presence of a generic steady wind. Along with the nonlinear model of the system, a process for trimming the airplane during flight considering the wind was developed. The output of the trim in windy conditions can be used as the initial conditions for the landing simulation.

The landing gear, instead, is a simplified anterior tricycle with each leg composed of a tire, modeled as a linear spring with a parallel damper and a nonlinear oleo-pneumatic shock absorber. A contact detection algorithm was also implemented to find when and which leg has touched the ground or rebounded. Once the contact between one or more legs and the ground is detected, the reaction forces are included in the simulation. Such reaction forces are modeled according to the usual simplified friction models. From the computation of the reaction forces and the motion of the aircraft on the ground, using the simple Achard theory, it was also possible to estimate the tire wear for each tire during landing.

The landing simulator model was tested with an airplane model inspired by the Lockheed Jetstar.

Next, the optimization of the tire wear due to the lateral drift during landing in crosswind conditions was performed. To do so, the simulation code was embedded inside an optimization algorithm with the aim of determining an optimal landing technique in terms of the sideslip angle before touchdown and control deflection after touchdown.

From the results obtained in this work and from extensive practice [39], the following conclusions can be derived:

- The landing simulator model is able to handle and combine airborne and ground landing phases considering generic wind conditions. The simulation, being based on a nonlinear three-dimensional model of airplane dynamics, is also compliant with the physics of the landing maneuver and considers the asymmetric contact among the wheels and the terrain, which is typically involved during crosswind conditions.
- A simulation parametric study shows that touchdowns at lower approach speeds and lower vertical speeds are associated with lower tire wear. This fact, which is expected, is due to lower lateral forces generated during the contact between the legs and ground, which lead to reduced wear.
- From the parametric analysis, it was also possible to show that in crosswind landing specific control settings after touchdown may reduce wear: the minimum wear is obtained if ailerons are deflected towards the upwind direction after touchdown, whereas the rudder is set near the trim conditions, maintaining a crossed-controls setting.
- A three-variable optimization problem aimed at finding the sideslip angle at trim and the lateral–directional controls after touchdown associated with the minimum tire wear can also be formulated. It was demonstrated that a mild track misalignment due to a difference between the airplane heading and runway direction is associated with reduced tire wear. In fact, even if this misalignment produces higher wear during the first instants after the first wheel touches the ground, the combination of the lateral forces on all legs, the motion of the aircraft once landed, and the initial airplane misalignment generates lower wear over the landing.

Clearly such promising but still preliminary results need further analysis before they can be considered consolidated. In terms of the extension of the optimization of tire wear, in fact, it could be interesting to consider different airplanes with different dimensions and weights. Moreover, since the analysis of this paper has focused on lateral friction, and, hence, on the wear due to lateral wheel drift, a complete study including the wheel spin-up, longitudinal friction, and brakes should be performed. In fact, including the longitudinal wear in the merit function may possibly allow one to seek the optimal longitudinal controls along with lateral–directional ones.

Finally, as far as the landing simulator is concerned, possible improvements may include the development of a control system capable of handling the whole landing maneuver from descent to airplane stop and the enrichment of the modeling of the aircraft aerodynamics, possibly including different flap settings.

Author Contributions: S.C. and C.E.D.R. developed the original formulation and composed the present paper. E.G. contributed to the refinement of the formulation, carried out the quantitative analyses, and contributed to the writing of the present paper. All authors participated equally in the development of the body of the work, with discussions and critical comments on the results. All authors have read and agreed to the published version of the manuscript.

Funding: This research received no external funding.

Institutional Review Board Statement: Not applicable.

Informed Consent Statement: Not applicable.

Data Availability Statement: All the data and the numerical tools used in this work may be obtained by contacting the corresponding authors.

Conflicts of Interest: The authors declare no conflict of interest.

Nomenclature

$\mathcal{B}$	Body reference frame
$\mathcal{N}$	NED (north–east–down) reference frame
$\overline{\mathcal{N}}$	Navigational reference frame
$\mathcal{S}$	Strut reference frame
$\mathcal{T}$	Tire reference frame
$\boldsymbol{b}_1, \boldsymbol{b}_2, \boldsymbol{b}_3$	Unit vectors of body frame
$\boldsymbol{e}_{321}$	Euler angles of sequence 3–2–1
$\boldsymbol{f}_\mathrm{a}, \boldsymbol{m}_{\mathrm{a}G}$	Aerodynamic force and moment about the gravity center
$\boldsymbol{f}_f$	Gravitational force
$\boldsymbol{f}_\mathrm{g}$	Gravitational force
$\boldsymbol{f}_\mathrm{r}, \boldsymbol{m}_{\mathrm{r}G}$	Reaction force and moment about the gravity center
$\boldsymbol{n}_1, \boldsymbol{n}_2, \boldsymbol{n}_3$	Unit vectors of NED frame
$\boldsymbol{q}$	Array with landing optimization parameters
$\boldsymbol{q}_\mathrm{L}, \boldsymbol{q}_\mathrm{U}$	Lower and upper bounds on optimization parameters
$\boldsymbol{r}_{A,B}$	Position of generic point A with respect to the generic point B
$\boldsymbol{s}_1, \boldsymbol{s}_2, \boldsymbol{s}_3$	Unit vectors of strut frame
$\boldsymbol{t}_1, \boldsymbol{t}_2, \boldsymbol{t}_3$	Unit vectors of strut frame
$\boldsymbol{x}_G$	Position of the center of gravity of the aircraft
$\boldsymbol{x}_\mathrm{trim}$	Unknown vector of the trim problem
$\boldsymbol{J}_G$	Inertia tensor about the gravity center
$\boldsymbol{R}_{321}$	Rotation tensor associated with Euler angles of sequence 3–2–1
$\boldsymbol{S}_{321}$	Tensor that links the rates of Euler angles with the angular velocity
$\boldsymbol{v}$	Aircraft linear velocity
$\boldsymbol{v}_C$	Velocity of the tire at the contact point
$\boldsymbol{v}_\mathrm{a}$	Airspeed
$\boldsymbol{v}_\mathrm{w}$	Wind speed
$\boldsymbol{\delta}$	Control input array, $\boldsymbol{\delta} = \{\delta_\mathrm{T}, \delta_\mathrm{E}, \delta_\mathrm{A}, \delta_\mathrm{R}\}^T$
$\boldsymbol{\omega}$	Aircraft angular velocity
A_c	Cross-section area of the cylinder
A_o	Equivalent orifice cross-section area
C	Tire contact point
F_{gas}	Elastic force of the shock absorber
F_{oil}	Damping force of the shock absorber
G	Center of gravity
G_0	Projection of the airplane center of gravity onto the ground
H	Hardness of the worn material
M	Mass of the aircraft
$f_{C_z}^{\mathcal{T}}$	Vertical force on tire contact point
$O_{\mathcal{S}}$	Origin of the strut reference frame
$O_{\mathcal{T}}$	Origin of the tire reference frame
V_0	Shock absorber internal volume
W_f	Work of the dissipation forces
W_x, W_y	Work of the longitudinal and lateral dissipation forces
c_d	Discard coefficient of the orifice of the shock absorber
c_t	Tire equivalent damping coefficient
k_a	Abrasion factor
k_t	Tire equivalent stiffness coefficient
$p(\beta, \delta_A, \delta_R, \phi, \psi)$	Piloting condition

p_o	Cylinder preload pressure
$v^{\mathcal{T}}_{C_x}$, $v^{\mathcal{T}}_{C_y}$	Longitudinal and lateral component of tire contact point velocity
t_{TD}, t_{end}	Touchdown and end of landing instants
α	Angle of attack
β	Sideslip angle
γ	Climb angle
γ_{gas}	Polytropic coefficient of the gas of the shock absorber
δ_s	Absorber stroke
δ_t	Tire deflection
δ_{T}	Throttle position
δ_{E}	Elevator deflection
δ_{A}	Aileron deflection
δ_{R}	Rudder deflection
θ	Pitch angle
μ_x,μ_y	Longitudinal and lateral tire friction coefficients
ρ_{oil}	Density of the oil of the shock absorber
τ	Skid angle related to the tire motion on the ground
ϕ	Roll angle
χ	Track angle
χ_{RNW}	Ground track orientation
ψ	Heading angle
ΔV	Volume of the worn material of the tire

Appendix A. Reference Aircraft Data Inspired by Lockheed Jetstar

The reference airplane data used in this work are reported in Tables A1–A4. The main sources from which the data were gathered are as follows:

- Technical reports, [26–28];
- Flight mechanics and aircraft design and system textbooks, [29,31,40,41];
- Scaled drawings (used when more accurate geometric data were unavailable);
- Supplier catalogues, [32].

Whenever real aircraft data were unavailable, aircraft preliminary design methods were applied in order to retrieve the missing information.

Unless otherwise specified, data refer to a *power approach* configuration, which includes a light gross weight, landing gear extended, 40% flaps, and sea-level conditions.

Table A1. Lockheed Jetstar geometric and inertial properties.

Property	Value	Unit
Wing area, S	50.39	m^2
Wing span, b	16.38	m
Mean aerodynamic chord, MAC	3.33	m
Center of gravity longitudinal position, x_{CG}	25% MAC	-
Airplane mass, M	10,842.67	kg
Inertia moment about $\boldsymbol{x}^{\mathrm{B}}$, I_x	57,314.48	kg m^2
Inertia moment about $\boldsymbol{y}^{\mathrm{B}}$, I_y	170,967.25	kg m^2
Inertia moment about $\boldsymbol{z}^{\mathrm{B}}$, I_z	217,071.83	kg m^2
Inertia moment with respect to plane $\boldsymbol{x}^{\mathrm{B}}\boldsymbol{z}^{\mathrm{B}}$, I_{xz}	7416.32	kg m^2

Table A2. Lockheed Jetstar aerodynamic properties.

Property	Value	Unit
Reference speed, U_0	68.05	$\frac{\mathrm{m}}{\mathrm{s}}$
Reference Mach, M	0.2	-
Reference angle of attach, α_0	0.0	deg
C_{L_0}	1.11	-
C_{D_0}	0.102	-
C_{L_α}	5.70	rad^{-1}
C_{D_α}	0.66	rad^{-1}
$C_{\mathcal{M}_\alpha}$	-1.26	rad^{-1}
$C_{L_{\dot{\alpha}}}$	-6.7	$\left(\frac{\mathrm{rad}}{\mathrm{s}}\right)^{-1}$
$C_{\mathcal{M}_{\dot{\alpha}}}$	-3.2	$\left(\frac{\mathrm{rad}}{\mathrm{s}}\right)^{-1}$
$C_{\mathcal{L}_q}$	5.4	$\left(\frac{\mathrm{rad}}{\mathrm{s}}\right)^{-1}$
$C_{\mathcal{M}_q}$	-20.8	$\left(\frac{\mathrm{rad}}{\mathrm{s}}\right)^{-1}$
C_{L_M}	-0.81	$\left(\frac{\mathrm{rad}}{\mathrm{s}}\right)^{-1}$
C_{D_M}	0.0	-
$C_{\mathcal{M}_M}$	0.27	-
$C_{L_{\delta_E}}$	0.338	rad^{-1}
$C_{\mathcal{M}_{\delta_E}}$	-1.34	rad^{-1}
C_{Y_β}	-0.96	rad^{-1}
$C_{\mathcal{L}_\beta}$	-0.221	rad^{-1}
$C_{\mathcal{N}_\beta}$	0.150	rad^{-1}
$C_{\mathcal{N}_p}$	-0.45	$\left(\frac{\mathrm{rad}}{\mathrm{s}}\right)^{-1}$
$C_{\mathcal{N}_p}$	-0.121	$\left(\frac{\mathrm{rad}}{\mathrm{s}}\right)^{-1}$
$C_{\mathcal{L}_r}$	0.101	$\left(\frac{\mathrm{rad}}{\mathrm{s}}\right)^{-1}$
$C_{\mathcal{N}_r}$	-0.30	$\left(\frac{\mathrm{rad}}{\mathrm{s}}\right)^{-1}$
$C_{\mathcal{L}_{\delta_A}}$	0.461	rad^{-1}
$C_{\mathcal{N}_{\delta_A}}$	0.0064	rad^{-1}
$C_{Y_{\delta_R}}$	0.175	rad^{-1}
$C_{\mathcal{L}_{\delta_R}}$	0.007	rad^{-1}
$C_{\mathcal{N}_{\delta_R}}$	-0.109	rad^{-1}

Table A3. Lockheed Jetstar main landing gear properties.

Property	Value	Unit
Main gear longitudinal position with respect to CG, $x^{\mathcal{B}}_{\mathcal{S}_{\mathrm{MG}}}$	-1	m
Main gear lateral position with respect to CG, $y^{\mathcal{B}}_{\mathcal{S}_{\mathrm{MG}}}$	± 1.92	m
Main gear vertical position with respect to CG in body axes, $z^{\mathcal{B}}_{\mathcal{S}_{\mathrm{MG}}}$	0.61	m
Main gear leg assembly mass, m_{MG}	300	kg
Main gear shock absorber stroke, $\delta_{s_{\mathrm{MG}}}$	0.30	m
Main gear shock absorber length, $L_{s_{0_{\mathrm{MG}}}}$	1.05	m
Main gear shock absorber cyclinder diameter, $d_{c_{\mathrm{MG}}}$	0.11	m
Main gear shock absorber orifice diameter, $d_{o_{\mathrm{MG}}}$	0.007	m
Main gear shock absorber preload pressure, $p_{0_{\mathrm{MG}}}$	$1 \cdot 10^6$	Pa
Main gear shock absorber internal volume, $V_{0_{\mathrm{MG}}}$	0.0034	m^3

Table A3. *Cont.*

Property	Value	Unit
Orifice discharge coefficient, c_d	0.61	-
Main gear tire undeformed radius, $r_{t0_{\mathrm{MG}}}$	0.32	m
Main gear tire equivalent stiffness, $k_{t_{\mathrm{MG}}}$	$1.1 \cdot 10^6$	$\frac{\mathrm{N}}{\mathrm{m}}$
Main gear tire equivalent damping, $c_{t_{\mathrm{MG}}}$	$4.34 \cdot 10^3$	$\frac{\mathrm{N}}{\mathrm{m/s}}$

Table A4. Lockheed Jetstar nose landing gear properties.

Property	Value	Unit
Nose gear longitudinal position with respect to CG, $x^{\mathcal{B}}_{\mathcal{S}_{\mathrm{NG}}}$	4.40	m
Nose gear lateral position with respect to CG, $y^{\mathcal{B}}_{\mathcal{S}_{\mathrm{NG}}}$	0	m
Nose gear vertical position with respect to CG, $z^{\mathcal{B}}_{\mathcal{S}_{\mathrm{NG}}}$	0.51	m
Nose gear leg assembly mass, m_{NG}	300	kg
Nose gear shock absorber stroke, $\delta_{s_{\mathrm{NG}}}$	0.30	m
Nose gear shock absorber length, $l_{s_{\mathrm{NG}}}$	1.15	m
Nose gear shock absorber cyclinder diameter, $d_{c_{\mathrm{NG}}}$	0.095	m
Nose gear shock absorber orifice diameter, $d_{o_{\mathrm{NG}}}$	0.006	m
Nose gear shock absorber preload pressure, $p_{0_{\mathrm{NG}}}$	$0.5 \cdot 10^6$	Pa
Nose gear shock absorber internal volume, $V_{0_{\mathrm{NG}}}$	0.0021	m^3
Orifice discharge coefficient, c_d	0.61	-
Nose gear tire undeformed radius, $r_{t0_{\mathrm{NG}}}$	0.25	m
Nose gear tire equivalent stiffness, $k_{t_{\mathrm{NG}}}$	$1.04 \cdot 10^6$	$\frac{\mathrm{N}}{\mathrm{m}}$
Nose gear tire equivalent damping, $c_{t_{\mathrm{NG}}}$	$2.85 \cdot 10^3$	$\frac{\mathrm{N}}{\mathrm{m/s}}$

References

1. Aibus S.A.S. *A Statistical Analysis of Commercial Aviation Accidents, 1958–2021*; Technical Report; Airbus: Blagnac, France, 2021.
2. Riboldi, C.E.D.; Cacciola, S.; Ceffa, L. Studying and Optimizing the Take-Off Performance of Three-Surface Aircraft. *Aerospace* **2022**, *9*, 139. [CrossRef]
3. Bottasso, C.L.; Croce, A.; Leonello, D.; Riviello, L. Optimization of Critical Trajectories for Rotorcraft Vehicles. *J. Am. Helicopter Soc.* **2005**, *50*, 165–177. [CrossRef]
4. Trainelli, L.; Gennaretti, M.; Bernardini, G.; Rolando, A.; Riboldi, C.E.D.; Redaelli, M.; Riviello, L.; Scandroglio, A. Innovative helicopter in-flight noise monitoring systems enabled by rotor-state measurements. *Noise Mapp.* **2016**, *3*, 190–215. [CrossRef]
5. Riboldi, C.E.D.; Rolando, A. Layout Analysis and Optimization of Airships with Thrust-Based Stability Augmentation. *Aerospace* **2022**, *9*, 393. [CrossRef]
6. Dreier, M.E. *Introduction to Helicopter and Tiltrotor Simulation*; AIAA (American Institute of Aeronautics and Astronautics): Reston, VA, USA, 2007.
7. Evans, P.E. Modeling and Simulation of Tricycle Landing Gear at Normal and Abnormal Conditions. Master's Thesis, West Virginia University, Morgantown, WV, USA, 2010. Available online: https://researchrepository.wvu.edu/etd/2153 (accessed on 10 May 2023).
8. Wang, C.; Holzapfel, F. Modeling of the Aircraft Landing Behavior for Runway Excursion and Abnormal Runway Contact Analysis. In Proceedings of the 2018 AIAA Modeling and Simulation Technologies Conference, Kissimmee, FL, USA, 8–12 January 2018. [CrossRef]
9. Daniels, J.N. *A Method for Landing Gear Modeling and Simulation with Experimental Validation*; Technical Report, NASA Contractor Report 201601; NASA Langley Research Center: Hampton, VA, USA, 1996.
10. Yang, X.; Yang, J.; Zhang, Z.; Ma, J.; Sun, Y.; Liu, H. A review of civil aircraft arresting system for runway overruns. *Prog. Aerosp. Sci.* **2018**, *102*, 99–121. [CrossRef]
11. Barnes, A.; Yager, T. *Enhancement of Ground Handling Simulation Capability*; Agard–AG–333; Advisory Group for Aerospace Research and Development, North Atlantic Treaty Organization: Neuilly sur Seine, France, 1998.
12. Vechtel, D. How future aircraft can benefit from a steerable main landing gear for crosswind operations. *CEAS Aeronaut. J.* **2019**, *11*, 417–429. [CrossRef]
13. Vechtel, D.; Meissner, U.; Hahn, K. On the use of a steerable main landing gear for crosswind landing assistance. *CEAS Aeronaut. J.* **2014**, *5*, 293–303. [CrossRef]

14. Shepherd, A.; Catt, T.; Cowlind, D. The simulation of aircraft landing gear dynamics. In Proceedings of the 18th Congress of the International Council of the Aeronautical Sciences, Beijing, China, 20–25 September 1992.
15. Evans, P.; Perhinschi, M.; Mullins, S. Modeling and Simulation of a Tricycle Landing Gear at Normal and Abnormal Conditions. In Proceedings of the AIAA Modeling and Simulation Technologies Conference, Toronto, ON, Canada, 2–5 August 2010. [CrossRef]
16. Lei, Z.; Hongzhou, J.; Hongren, L. Object-oriented landing gear model in a PC-based flight simulator. *Simul. Model. Pract. Theory* **2008**, *16*, 1514–1532. [CrossRef]
17. Wen, Z.; Zhi, Z.; Qidan, Z.; Shiyue, X. Dynamics Model of Carrier-based Aircraft Landing Gears Landed on Dynamic Deck. *Chin. J. Aeronaut.* **2009**, *22*, 371–379. [CrossRef]
18. Alroqi, A.; Wang, W. Comparison of Aircraft Tire Wear with Initial Wheel Rotational Speed. *Int. J. Aviat. Aeronaut. Aerosp.* **2015**, *2*, 2. [CrossRef]
19. Reye, K. Zur Theorie der Zapfenreibung [On the theory of pivot friction]. *Der Civilingenieur* **1860**, *4*, 235–255.
20. Archard, J.F. Contact and Rubbing of Flat Surfaces. *J. Appl. Phys.* **1953**, *24*, 981–988. [CrossRef]
21. Sethuramiah, A.; Kumar, R. *Modeling of Chemical Wear: Relevance to Practice*; Elsevier: Amsterdam, The Netherlands, 2015; pp. 1–232.
22. Cacciola, S.; Riboldi, C.E.D.; Arnoldi, M. Three-surface model with redundant longitudinal control: Modeling, trim optimization and control in a preliminary design perspective. *Aerospace* **2021**, *8*, 139. .:10.3390/aerospace8050139. [CrossRef]
23. Riboldi, C.E.D.; Rolando, A. Thrust-Based Stabilization and Guidance for Airships without Thrust-Vectoring. *Noise Mapp.* **2023**, *10*, 344. [CrossRef]
24. Correia, D.; Ferreira A. Aircrafts on-ground dynamics models and simulation software: State-of-the-art. *Sustainability* **2021**, *13*, 9147. [CrossRef]
25. The MathWorks Inc. *MATLAB Version: R2022a*; The MathWorks Inc.: Natick, MA, USA, 2022. Available online: https://www.mathworks.com (accessed on 10 May 2023).
26. Clark, D.; Kroll, J. *General Purpose Airborne Simulator—Conceptual Design Report*; NASA Contractor Report 544; Cornell Aeronautical Lab.: Buffalo, NY, USA, 1966.
27. Heffley, R.; Jewell, W. *Aircraft Handling Qualities Data*; NASA Contractor Report 2144; System Technology, Inc.: Hawthorne, CA, USA, 1972.
28. Smith, H. *Flight-Determined Stability and Control Derivatives for and Executive Jet Transport*; NASA Technical Memorandum; NASA Flight Research Center: Edwards, CA, USA, 1975.
29. Roskam, J. *Airplane Design*; Number pt. 4 in Airplane Design; DARcorporation: Lawrence, KS, USA, 1985.
30. Torenbeek, E. *Synthesis of Subsonic Airplane Design*; Delft University Press: Delft, The Netherlands, 1982.
31. Currey, N. *Aircraft Landing Gear Design: Principles and Practices*; AIAA Education Series; American Institute of Aeronautics & Astronautics: Washington, DC, USA, 1988.
32. The Goodyear Tire & Rubber Company. *Goodyear Aviation Data Book*; The Goodyear Tire & Rubber Company: Akron, OH, USA, 2021.
33. De Marco, A.; Duke, E.; Berndt, J. A General Solution to the Aircraft Trim Problem. In Proceedings of the AIAA Modeling and Simulation Technologies Conference and Exhibit, Hilton Head, SC, USA, 20–23 August 2007. [CrossRef]
34. Muskardin, T. Autonomous Landing of Fixed-Wing Aircraft on Mobile Platforms. Ph.D. Thesis, Universidad de Sevilla, Departamento de Ingeniería de Sistemas y Automática, Sevilla, Spain, 2020.
35. Popov, V.L.; Heß, M.; Willert, E. *Handbook of Contact Mechanics*; Springer: Berlin/Heidelberg, Germany, 2019.
36. van der Veen, J. An Analytical Approach to Dynamic Irregular Tyre Wear. Master's Thesis, Eindhoven University of Technology, Department Mechanical Engineering, Eindhoven, The Netherlands, 2007.
37. Alroqi, A.; Wang, W. Reduction of Aircraft Tyre Wear by Pre-Rotating Wheel Using ANSYS Mechanical Transient. *Adv. Eng. Forum* **2016**, *17*, 89–100. [CrossRef]
38. MATLAB. *Optimization Toolbox User's Guide*; The MathWorks Inc.: Natick, MA, USA, 2022.
39. Generali, E. Airplane Landing Simulation and Tire Wear Optimization in Crosswind Conditions. Master's Thesis, Politecnico di Milano, Dipartimento di Scienze e Tecnologie Aerospaziali, Milan, Italy, 2022.
40. Nelson, R. *Flight Stability and Automatic Control*; WBC/McGraw-Hill: New York, NY, USA, 1989.
41. Sadraey, M.H. *Aircraft Design: A Systems Engineering Approach*; Aerospace Series; John Wiley and Sons: Chichester, UK, 2012.